Hydrophobic binary mixtures containing amphotericin B as lipophilic solutions for the treatment of cutaneous leishmaniasis

Luc Augis, Canh Hung Nguyen, Cécile Ciseran, András Wacha, Françoise Mercier-Nomé, Séverine Domenichini, Christina Sizun, Sophie Fourmentin, François-Xavier Legrand

International Journal of Pharmaceutics 662 (2024) 124486

Contents lists available at ScienceDirect

International Journal of Pharmaceutics

journal homepage: www.elsevier.com/locate/ijpharm

Hydrophobic binary mixtures containing amphotericin B as lipophilic solutions for the treatment of cutaneous leishmaniasis

Luc Augis [a], Cảnh Hưng Nguyễn [a,b], Cécile Ciseran [a], András Wacha [c], Françoise Mercier-Nomé [d,e], Séverine Domenichini [d], Christina Sizun [f], Sophie Fourmentin [g], François-Xavier Legrand [a,*]

[a] Université Paris-Saclay, CNRS, Institut Galien Paris-Saclay, 91400 Orsay, France
[b] Department of Pharmaceutics, Hanoi University of Pharmacy, 13-15 Le Thanh Tong, Hoan Kiem, Hanoi, Viet Nam
[c] Research Centre for Natural Sciences, Institute of Materials and Environmental Chemistry, Magyar tudósok körútja 2, Budapest H-1117, Hungary
[d] Université Paris-Saclay, Inserm, CNRS, Ingénierie et Plateformes au Service de l'Innovation Thérapeutique, 91400 Orsay, France
[e] Université Paris-Saclay, Inserm, Inflammation, Microbiome et Immunosurveillance, 91400 Orsay, France
[f] Université Paris-Saclay, CNRS, Institut de Chimie des Substances Naturelles, UPR 2301, 91198 Gif-sur-Yvette, France
[g] Univ. Littoral Côte d'Opale, UR 4492, UCEIV, Unité de Chimie Environnementale et Interactions sur le Vivant, 59140 Dunkerque, France

ARTICLE INFO

Keywords:
Cutaneous leishmaniasis
Amphotericin B
Deep eutectic solvents
Low transition temperature mixtures
Lipophilic solution
MTT assay
Franz diffusion cells

ABSTRACT

Cutaneous leishmaniasis, caused by Leishmania parasites, requires treatments with fewer side effects than those currently available. The development of a topical solution based on amphotericin B (AmB) was pursued. The considerable interest in deep eutectic solvents (DESs) and their remarkable advantages inspired the search for a suitable hydrophobic excipient. Various mixtures based on commonly used hydrogen bond donors (HBDs) and acceptors (HBAs) for DES preparations were explored. Initial physical and *in-vitro* screenings showed the potential of quaternary phosphonium salt-based mixtures. Through thermal analysis, it was determined that most of these mixtures did not exhibit eutectic behavior. X-ray scattering studies revealed a sponge-like nanoscale structure. The most promising formulation, based on a combination of trihexyl(tetradecyl)phosphonium chloride and 1-oleoyl-*rac*-glycerol, showed no deleterious effects through histological evaluation. AmB was fully solubilized at concentrations between 0.5 and 0.8 mg·mL^{-1}, depending on the formulation. The monomeric state of AmB was observed by circular dichroism. *In-vitro* irritation tests demonstrated acceptable viability for AmB-based formulations up to 0.5 mg·mL^{-1}. Additionally, an *ex-vivo* penetration study on pig ear skin revealed no transcutaneous passage, confirming AmB retention in healthy, unaffected skin.

1. Introduction

Leishmaniasis is a tropical infection caused by the *Leishmania* species of parasites, transmitted through sandfly bites. It manifests in various clinical forms, including cutaneous leishmaniasis (CL), visceral leishmaniasis (VL), and mucocutaneous leishmaniasis (MCL). CL is the most widespread, with over 220,000 new cases reported in 2021. The World Health Organization (WHO) estimates more than 1 million new cases occurring annually, with no evidence of decline (Leishmaniasis, 2023). CL predominantly affects countries in the Middle East and Latin America countries, with significant percentages of case in Syria (35 %), Afghanistan (18 %), Pakistan (8 %), Brazil (7 %), Iran (6 %), and Iraq (6 %), cumulatively accounting for 80 % of the reported cases in 2021. Recognized by the WHO as a neglected tropical disease, leishmaniasis significantly impacts public health but lacks adequate attention and resources for the development of effective and affordable treatments.

CL lesions, while having the potential to self-heal, often result in disfiguring scars, causing both physical and emotional distress, and societal stigma. Moreover, in some cases, even after skin ulcers have healed, the condition can progress over months or years. The spread of parasites often leads to MCL, bringing further degradations of mucous membranes in the naso-oropharyngeal region, mouth, and nose (Latest Trends in Zoology and Entomology Sciences, 2023).

Existing treatments for CL all have limitations and can induce significant side effects. The first-line treatment involves pentavalent antimony derivatives, such as meglumine antimoniate and sodium

* Corresponding author.
E-mail address: francois-xavier.legrand@universite-paris-saclay.fr (F.-X. Legrand).

https://doi.org/10.1016/j.ijpharm.2024.124486
Received 9 February 2024; Received in revised form 6 July 2024; Accepted 16 July 2024
Available online 19 July 2024

stibogluconate (Comité, 2011). These compounds are typically administered as injections into the bloodstream, muscles, or directly into the lesion sites (Siadat et al., 2023; Reithinger et al., 2005). Although effective, especially at higher doses (20 mg·kg^{-1} daily for 20 days) (Wortmann et al., 2002; Berman, 1997), these treatments can cause serious complications such as renal failure and liver toxicity (Reithinger et al., 2007). Moreover, the discomfort of daily injections often results in patients discontinuing their treatment prematurely.

Amphotericin B (AmB), the second-line treatment, is particularly used in cases of antimonial resistance. As a powerful antifungal drug, AmB forms oligomers in aqueous solutions which are highly effective but also lead to severe toxic side effects (Espada et al., 2008). Despite attempts to reduce toxicity through formulations with sodium deoxycholate (Fungizone®) and lipid-based formulations (Ambisome®, Amphocil®, Abelcet®), challenges remain due to the need for parenteral administration, high production costs, and the need for hospitalization (Faustino and Pinheiro, 2020). Other treatments such as oral miltefosine, parenteral paromomycin, and pentamidine isethionate also carry risks of systemic toxicity. To mitigate this, topical formulations of paromomycin, initially at 15 % concentration, were developed at the end of the 1980s (El-On et al., 1988; El-Safi et al., 1990). Currently, the WHO recommends a formulation of paromomycin with 12 % methylbenzethonium chloride as the only topical drug treatment for CL (Comité, 2011).

Considering these challenges, the discovery in 2003 of deep eutectic solvents (DESs) by Abbott et al. (2003) has attracted interest. DESs are valued for their reusability, non-volatility, biodegradability, and relatively low toxicity (Radošević et al., 2015; Radošević et al., 2018; Juneidi et al., 2016; Li et al., 2016; Gano et al., 2017; Chen et al., 2021; Dietz et al., 2019; Abbott et al., 2004). These liquid mixtures, formed by combining Lewis or Brønsted acids and bases, form a hydrogen-bonding network, resulting in a eutectic mixture with significant depression compared to the ideal eutectic behavior (Abranches and Coutinho, 2023). DESs are widely used in various fields due to their ease of preparation and versatility (Rente et al., 2022; Makoś et al., 2020; Mannu et al., 2021; Hansen et al., 2021; Smith et al., 2014; Zubeir et al., 2018; Cruz et al., 2017; Deep Eutectic Solvents for Medicine, 2021).

The introduction of hydrophobic DESs (HDESs) in 2015 (Van Osch et al., 2015; Ribeiro et al., 2015) marked a significant advancement, particularly in extracting pollutants (AlOmar et al., 2017; Phelps et al., 2018; Florindo et al., 2017; Yang et al., 2019; Ge et al., 2019; AlOmar et al., 2016) and drugs (Rajabi et al., 2019; Shishov et al., 2018; Cao et al., 2017; Rajabi et al., 2018; Tang et al., 2018). Despite their unique benefits, HDESs have been studied less than hydrophilic DESs (Makoś et al., 2020). Typically, HDESs are made of quaternary ammonium or phosphonium salts as hydrogen bond acceptors (HBAs) and phenols, alcohols, or carboxylic acids as hydrogen bond donors (HBDs) (Makoś et al., 2020). HDESs are best for their water-repellency (Ge et al., 2019; Florindo et al., 2014; Diogo et al., 2014; Du et al., 2016; Khataei et al., 2018; Wang et al., 2017) and hydrophobicity, which can be tailored through chain length modifications (Florindo et al., 2018; Dwamena and Raynie, 2020). These characteristics make them particularly suitable for extraction and purification applications. However, their potential in drug delivery, especially in dermatological applications, remains largely unexplored.

This study aims to exploit the innovative properties of HDESs in combination with the established efficacy of AmB to develop a topical CL treatment. This approach seeks to address the limitations of existing therapies, offering an affordable, less toxic, and easy-to-apply option. Furthermore, a HDES-AmB solution might also be efficient in treating fungal skin infections, such as mold-induced onychomycosis (Chabasse and Pihet, 2014; Feuilhade De Chauvin, 2014) demonstrating its versatility and potential in dermatology. Briefly, we identified the most suitable solvents for topical applications from the diverse range of HDES starting materials documented in the literature, through thermal and physicochemical evaluations before assessing their capability to effectively solubilize and deliver AmB.

2. Materials and methods

2.1. Materials

Tetrabutylphosphonium chloride, tetraoctylammonium chloride, methyltrioctylammonium chloride, tetrabutylammonium chloride, tetrabutylphosphonium, octanoic acid, decanoic acid, dodecanoic acid, tetradecanoic acid, hexadecanoic acid, octadecanoic acid, tetradecan-1-ol, octadecan-1-ol, sodium dodecyl sulfate (≥98.5 %), Dulbelcco's Phosphate Buffered Saline, *n*-decane (99 %), thiazolyl blue tetrazolium bromide (98 %), Nile Red (≥97 %), dimethylsulfoxide (DMSO), tetrahydrofuran (THF), acetonitrile (AcN), triethylamine (≥99.5 %) and fluorescein isothiocyanate–dextran (average mol wt. 4000) were purchased from Sigma-Aldrich (Saint-Quentin Fallavier, France). Decan-1-ol and hexadecan-1-ol were gifts from Stearinerie Dubois (Boulogne-Billancourt, France). Trihexyl(tetradecyl)phosphonium chloride and trihexyl(octyl)phosphonium chloride were purchased from Strem Chemicals (USA). Amphotericin B from *Streptomyces nodosus* was purchased from Alfa Aesar (Heysham, UK). Dodecan-1-ol was purchased from Acros Organics (Belgium). 1-Oleoyl-*rac*-glycerol (monoolein) was purchased from Nu-Chek Prep, Inc. (USA). Purities of the starting materials in the mixtures are reported in Table S1. Ultrapure water (surface tension $\gamma = 72.2$ mN.m^{-1} at 22 °C; resistivity = 18.2 MΩ·cm) was produced by a Millipore Milli-Q Direct 8 water purification system.

2.2. Hydrophobic mixture preparation

All mixtures were prepared by mixing the two components (HBA and HBD) in a 40-mL glass vial. All ratios are molar ratios and are specified below, if a ratio 1:1 was not used. The weight measurements were done using digital weighing scales (Mettler Toledo XS105) with an accuracy of 10^{-5} g. Components were used without prior purification. The vials were then heated to 50 °C in an oil-containing crystallizer, until a clear and homogeneous mixture was obtained. During the heating period, the vials were periodically vortexed for a few seconds for homogenization. The monoolein mixture was heated to 30 °C to prevent any degradation.

2.3. Irritation assessment

An epidermal tissue model EpiDerm™ (MatTek IVLSL, Bratislava, Slovakia) was used for irritation tests. OECD 439 guidelines for *in-vitro* skin irritation on reconstructed human epidermis were followed (OECD, 2021). Each EpiDerm™ tissue was treated topically with 30 µL (equivalent to 50 µL·cm^{-2}) of mixture, or with Dulbecco's phosphate-buffered saline (DPBS) as a negative control, or 5 % sodium dodecyl sulfate (SDS) as a positive control. After 1 h of exposure, epidermal surface was rinsed with DPBS according to the manufacturer's instructions. Then, the epidermis cultured for another 42 h in order to allow recovery of the tissues from any harmful but reversible effects. Then, the MTT assay (MTT-100, MatTek IVLSL) was carried out as per the manufacturer's instructions. The % viability of individual tissues was determined by the equation: Viability (%) = 100 × [OD(sample)/OD(negative control)] where OD is optical density.

2.4. Differential scanning calorimetry (DSC)

Differential scanning calorimetry (DSC) experiments were carried out using a Perkin-Elmer DSC Diamond apparatus purged with N_2 flow (20 mL·min^{-1}) and equipped with an Intracooler 2P cooling device and connected to a Pyris Thermal Analysis Software System (version 13.2.1). 10 µL of the sample was introduced in a 50-µL aluminum capsule using a micropipette. The sample mass was recorded using digital scales (Mettler Toledo XS105) with an accuracy of 10^{-5} g. The lid was then hermetically sealed onto the capsule using a press. The program used started with an equilibration at 25 °C for 5 min, followed by a cooling step at 10 °C·min^{-1} and a heating step at 10 °C·min^{-1}. These steps were followed by successive

cooling cycles set at 10 °C·min^{-1} alternating with heating cycles at 20 °C·min^{-1}, 15 °C·min^{-1}, 10 °C·min^{-1} then 5 °C·min^{-1}. Four different cycle speeds were used to estimate the transition temperatures (T_{ONSET} and T_{END}) by extrapolating to zero speed. Reference samples (*n*-decane, purified water, cyclohexane, gallium, naphthalene and biphenyl) were used to correct the values. This procedure was carried out for reference samples and each mixture ratio (from 1:9 to 9:1).

2.5. Low-temperature Differential Scanning Calorimetry (DSC)

The thermal behavior of the prepared samples was evaluated using the TA Instruments DSC 2500 calorimeter equipped with an intracooler RCS90. Approximately 5 mg of the sample was placed in a Tzero Aluminum Hermetic capsule of 50 µL capacity. The capsule lid was hermetically sealed using a press. The program started with an equilibration phase at −90 °C for 2 min, followed by a heating phase from −90 °C to 60 °C at a rate of 5 °C·min^{-1}. Subsequently, a second cycle was carried out, starting from 25 °C to −90 °C at 5 °C·min^{-1}, maintaining an isotherm at −90 °C for 5 min, and concluding with a final heating step from −90° to 60 °C. The helium flow rate was set at 50 mL·min^{-1}.

2.6. Thermogravimetric analysis (TGA)

Thermogravimetric analysis (TGA) was performed using the TA Instruments TGA 550. Approximately 5 mg of the sample was introduced into a 100-µL platinum capsule. The program used started at room temperature (around 25 °C) and ramped to 550 °C at a rate of 5 °C·min^{-1}. under a nitrogen gas atmosphere (60 mL·min^{-1}). The onset temperature (T_{ONSET}) was determined as the intersection of the baseline weight and the tangent of the weight dependence on the temperature curve, representing the point where the maximum decomposition rate occurs.

2.7. Small- and Wide-Angle X-ray scattering (SWAXS)

Experiments were carried out on the CREDO instrument (Wacha et al., 2014), equipped with a Genix3D Cu ULD type X-ray source (Xenocs SA, Sassenage, France) producing a nearly parallel Cu Kα radiation ($\lambda = 1.54$ Å) due to the parabolic optics coupled to the X-ray tube. The divergence and shape of the beam was defined using a three-pinhole collimation scheme (Wacha, 2015). Samples were filled into capillaries of ~1.5 mm outer diameter (~0.01 mm wall thickness, produced by WJM-Glas Müller GmbH, Berlin, Germany), sealed with hot glue to make them vacuum-tight and placed in a temperature-controlled aluminum block (25 °C), situated in the evacuated sample chamber of the instrument. Scattered X-rays were recorded using a Pilatus-300 k CMOS hybrid pixel detector at 135.8 and 528.7 mm sample-to-detector distance, covering a combined momentum transfer ($q = 4\pi \times \sin(\theta)/\lambda$, where 2θ is the scattering angle) range from 0.0195 to 1.9 Å^{-1}. Exposures were performed in 300-s units, repeated several times until satisfactory statistics were obtained. Each recorded scattering image was treated using the on-line data reduction algorithm of the instrument, subtracting external and instrumental backgrounds (dark and empty beam signals), correcting for detector flatness and sample self-absorption, as well as normalizing by exposure time. Additionally, the intensity scale was calibrated into instrument-independent units of differential scattering cross-section using a piece of Glassy Carbon (courtesy of J. Ilavsky, APS, Chicago, US). Repeated scattering patterns from each sample were analyzed and those which were found to be outliers were discarded. The remaining images were averaged, and after azimuthal integration of the final image, the scattering curve (intensity *vs.* q) was obtained.

2.8. Polarity assessment

2.8.1. Preparation of Nile Red solutions

Prior to assessing the polarity, a stock solution of Nile Red (6×10^{-3} mol·L^{-1}) was first prepared in chloroform. Then 1 mL of this solution was added to each empty vial. The chloroform was subsequently evaporated using a nitrogen flux and 1 mL of the specified mixture was added to the dried dye. The solution was thoroughly mixed using a vortex until the Nile Red was fully dissolved.

2.8.2. Spectroscopy UV–vis analysis

One milliliter of the sample was added to a quartz cuvette. A blank subtraction was performed beforehand on the same cuvette containing the studied mixture without Nile Red. The absorbance spectra of Nile Red in the mixtures were recorded between 400 and 750 nm using a PerkinElmer Lambda 35 spectrophotometer, with a wavelength resolution of 0.1 nm. The wavelength at which the maximum visible light absorption occurred was noted $\lambda_{max,NR}$.

2.9. Contact angle

The measurements were made using the Drop Shape Analyzer DSA 100 (Krüss). A Teflon plate was used as a deposit support for the drops. The samples were taken using a Hamilton syringe. Then the plunger was pushed little by little until a drop formed at the end of the needle and fell onto the support. The angle formed between the drop and the base line formed by the support was measured every 5 s for 2 min with the Drop Shape software. Measurements were conducted under constant conditions of temperature (20 ± 1 °C) and humidity. This operation was repeated at least 10 times for each sample. The median and the standard deviation for each series of measurements were then determined for the interpretation of the results.

2.10. Water content

The water content present in the studied mixtures and conventional solvents was determined by Karl Fischer method using a Mettler Toledo C20SX KF Titrator.

2.11. Density

The density of the studied mixtures was measured at 25, 32, 37, 44 and 50 °C at atmospheric pressure using an Anton Paar SVM 3001 apparatus. In order to fit the experimental density values, a linear fit was adopted using the following equation (Eq. (1)):

$$\rho = a + b \times T \quad (1)$$

where ρ corresponds to density in g·cm^{-3}, T is the temperature in Celsius and a (g·cm^{-3}) and b (g·cm^{-3}·°C^{-1}) are the fitting parameters that depend on the mixture. The adjustable parameters (a and b) were determined from the fitting of the experimental density data to Eq. (1). These values, along with R^2 and %AAD (Average Absolute Deviation) values, are reported in Table S2.

2.12. Viscosity

Dynamic viscosities were determined at 25, 32, 37, 44 and 50 °C, at atmospheric pressure, using an Anton Paar SVM 3001 apparatus. The experimental viscosity values were fitted as a function of temperature, using the Vogel − Fulcher − Tammann (VFT) model (Eq. (2)):

$$\eta = AT^{1/2} \exp\left(\frac{k}{T - T_0}\right) \quad (2)$$

where η (mPa.s) quantifies the viscosity, A (mPa·s·K$^{-1/2}$), k (K) and T_0 (K) are empirical constants. These values, along with %AAD values, are reported in Table S3.

2.13. Rheology

Measurements were carried out using an AR-G2 rheometer (TA Instruments). The program used began at 25 °C or 32 °C for 300 s. Then, the sample was sheared with a decreasing shear rate between 100.0 and 0.1 s^{-1} with 5 points per decade and 30 s of average duration. The shear rate was then set at 0.1 s^{-1} for 60 s. Finally, the sample was subjected to increasing shear rising from 0.1 to 100.0 s^{-1}. Each measurement was performed three times. Data processing was performed using Trios software. The geometry used was a steel truncated cone 40 mm in diameter with a truncation of 1.0°.

2.14. Histology

A 3D full thickness model of Human Skin, EpiDermFT™ (MatTek IVLSL, Bratislava, Slovakia), was used for histological studies. Each EpiDermFT™ tissue was treated topically with 50 µL (equivalent to 50 µL·cm^{-2}) of mixture or with Dulbecco's phosphate-buffered saline (DPBS) as a negative control. After 1 h of exposure, the epidermal surface was rinsed with DPBS according to the manufacturer's instructions. Then, EpiDermFT™ were fixed with 4 % PFA and embedded in paraffin. Sections (3 µm thick) were deparaffinized and were stained with hematoxylin and eosin (HE).

For immunofluorescence, slides were incubated overnight at 4 °C with primary antibodies diluted in 0.02 % Triton X-100 in PBS. Primary antibodies were as follows: rabbit anti-Ki67 (1:75; Abcam ab16667), mouse anti-filaggrin (1:100; Abcam ab218395), rabbit anti-TGM-1 (1:100; Proteintech 12912-3-AP), rabbit anti-Aquaporin-3 (1:100; Abcam ab153694), mouse anti-E-Cadherin (1:100; Abcam ab1416), mouse anti-Claudin-1 (1:200; Abcam ab242370), rabbit anti-Occludin (1:100; Abcam ab216327), rabbit anti-Cytokeratin 10 (1:100; Proteintech 18343-1-AP) and mouse anti-Cytokeratin 1 (1:200; Santa Cruz sc-376224). For immunofluorescence detection, secondary antibodies Alexa Fluor™ 488 goat anti-mouse (1:200; Invitrogen A11029), Alexa Fluor™ 488 donkey anti-rabbit (1:200; Invitrogen A21206), Alexa Fluor™ 594 goat anti-mouse (1:200; Invitrogen A32742) and Alexa Fluor™ 594 goat anti-rabbit (1:200; Invitrogen A32740) were used. To analyze apoptosis, autofluorescence was quenched by treating paraffin-embedded sections with PBS/BSA (5 %) for 2 h before performing TUNEL staining according to the manufacturer's protocol and using Proteinase K treatment (*In Situ* Death Detection Kit; Roche 11684795910). Slides were scanned using NanoZoomer 2.0-RS digital slide scanner (Hamamatsu, Japan). Images were digitally captured from the scanned slides using NDP.view2 software (Hamamatsu).

All image analysis was performed using FIJI software (Schindelin et al., 2012; Schneider et al., 2012). For fluorescence labeling analysis, we developed custom image-processing macros. These macros use the "free-hand selection" tool to define regions of interest, such as tissue or epidermis, and measure their areas. We also applied thresholding based on the fluorescence intensity in specific channels to quantify the labeling of interest.

To count nuclei (total with DAPI staining, positive in TUNEL or Ki67 labeling), additional processes are employed including Mask Creation, Gaussian Blur Filter, multiple Binary Processes, Image Calculator, and Analyze Particle. The thickness of the epidermis expressed in µm was measured on 6 fields (×20 magnification) of each sample using the NDP.view2 software (Hamamatsu). Finally, values were exported to Excel and Prism-GraphPad for conducting statistical analyses and creating graphical representations.

2.15. Solubility of Amphotericin B

2.15.1. Calibration curve

A stock solution of AmB (2495 µg·mL^{-1}) was prepared by dissolving 5 mg of AmB in 2 mL of tetrahydrofuran (THF). This stock solution was further diluted in THF to yield 6 different concentrations of AmB: 12.5, 6.2, 5, 3.3, 2.4, and 1.25 µg·mL^{-1}. Each of these standard solutions was prepared in duplicate.

2.15.2. Preparation of AmB samples

Taking into account the susceptibility of AmB to light and temperature, a preliminary investigation was carried out to establish the optimal temperature (18 or 35 °C) and duration of stirring, ranging from 1 to 48 h, to prevent the formation of degradation products. Amphotericin B samples were prepared by adding 1 mg of AmB to 1 mL of the study mixture. The mixture was homogenized for 16 h at 18 °C, shielded from light (under a cardboard box). Subsequently, 500 µL of the mixture was extracted for centrifugation at 3000*g* for 40 min at 18 °C. After centrifugation, 50 µL of the supernatant was diluted in 5 mL of tetrahydrofuran for analysis.

2.15.3. HPLC-DAD analysis

AmB was quantified using a ThermoScientific UltiMate 3000 UHPLC system equipped with a SRD-3600 solvent degasser, a DGP-3600RS dual-gradient pump, a WPS-3000TSL autosampler, a TCC-3000 thermostated column compartment and a DAD-3000 Diode Array Detector. A C18 chromatographic column (Waters Symmetry® C18, 5 µm, 4.6 × 150 mm) thermostated at 30 °C was used for separation. The following solutions were mixed to prepare the mobile phase: an aqueous solution containing 0.5 % triethylamine (TEA), adjusted to pH 5.2 using formic acid with acetonitrile (ACN) and tetrahydrofuran (THF) in a ratio of 13:5:2 (v/v/v). The flow rate was set at 0.4 mL·min^{-1}. These conditions resulted in a retention time of 11–12 min for AmB.

2.16. Evaluation of AmB aggregation state

UV–Vis spectroscopy and circular dichroism (CD) measurements were carried out on a Jasco J-810 spectropolarimeter using a 10-mm path length cell. The temperature was set to 25 °C, using a Peltier temperature controller. Spectra were recorded between 300 and 450 nm at a standard sensitivity. The scanning speed was 50 nm.min^{-1}, digital integration time 1 s, data pitch 0.2 nm, bandwidth 1.00 nm. Two scans were averaged per spectrum, smoothed with a Savitzky-Golay filter with a convolution width of 20, and baseline-corrected.

2.17. Ex-vivo skin penetration

2.17.1. Skin preparation

Fresh pig ear skin was acquired from Guy Harang slaughterhouse (Houdan, France) and promptly prepared within 10 h of the animal's demise. The outer skin layer was carefully detached from the ear using scalpels. The subcutaneous fat beneath the dermis was meticulously eliminated, ensuring the integrity of the skin. Subsequently, the skin was briefly cleansed in a phosphate buffer saline solution and then stored by freezing it at −80 °C.

2.17.2. Penetration test

An *ex-vivo* penetration test was conducted using Franz diffusion cells containing with pig ear skin. The test was carried out over 4 days, employing a diffusion area of 1.77 cm^2 and a volume of 7.5 mL in the lower compartment. The receptor compartment was filled with phosphate buffer (pH 7.4) without divalent ions and containing 1 % (w/v) of sodium lauryl sulfate. The cells were stirred at maximum speed, and the temperature was meticulously adjusted using a thermal camera. The bath temperature was maintained at 34.5 °C to ensure a cell temperature of 32 °C. The skin samples were placed between the donor and receptor compartments, with the epidermis facing the donor. After the deposition of 88 µL of the AmB formulations, the donor compartment was securely sealed with parafilm to prevent evaporation. Throughout the experiment, a vigilant check for air bubbles at the top of the receptor medium was conducted. If any were found, they were promptly removed, and the receptor volume was adjusted accordingly. At the end of the 96-hour

experiment, the receptor liquid was collected for spectroscopic analysis. The same procedure was followed for the preliminary test containing fluorescein isothiocyanate labeled dextran (4400 Da).

2.17.3. Quantification of AmB in the receptor compartment

3 mL of the receptor medium was frozen at −22 °C, followed by freeze-drying using a Cryotec freeze-dryer (France). The resulting residue was dissolved in 1 mL of dimethyl sulfoxide (DMSO) and then centrifuged at 3500*g* for 15 min. AmB was quantified using UV–vis spectroscopy in the range of 300–450 nm, using PerkinElmer Lambda 35 spectrophotometer with a wavelength resolution of 0.1 nm. Blank acquisitions were performed on the same cuvette containing the lyophilized 5 mL of the original receiving solution, dissolved in DMSO. Since no AmB band was identified regardless of the formulation used, a calibration range was not established.

2.18. Statistical analysis

Regarding cell viability experiments, unpaired *t*-test was used to determine the significance between the samples and controls. This analysis was conducted over three independent measurements using GraphPad Prism Software version 9.4.1. For staining and histological quantifications, we employed a one-way ANOVA followed by a Kruskal-Wallis multiple comparisons test.

3. Results and discussion

3.1. Mixture preparation

3.1.1. Starting material selection

We employed two approaches to select the starting materials. The first approach involved selecting hydrogen bond donors (HBDs) and hydrogen bond acceptors (HBAs) that, according to the literature, jointly form eutectic mixtures at specific ratios. The second approach was to choose HBAs and HBDs known for independently forming deep eutectic solvents (DESs) or low-transition-temperature mixtures (LTTMs) as reported in Table S1. For HBAs, we selected six ammonium or phosphonium salts with varying chain lengths. As HBDs, we chose a range of fatty acids (from C8 to C18) and fatty alcohols (from C10 to C16). Moreover, a patent has shown that combining monoolein (MO) with a phosphonium salt can form a LTTM (Patil and Bodige, 2016). Considering MO's role as chemical penetration enhancer (CPE) (Songkro, 2009) facilitating transdermal drug delivery, we also included this monoglyceride in the list of HBD candidates. Fig. 1 depicts the chemical structures of all the starting materials considered in this study, along with their respective acronyms.

3.1.2. Physical and irritation screening

The mixtures were prepared using the conventional stirring-heating method. Molar ratios were chosen from the literature, with a 1:1 ratio used for newly studied combinations. Mixtures that remained solid at room temperature or recrystallized after a few days were discarded, as detailed in Fig. S1. Next, the irritation level was assessed using a 3D reconstructed human epidermis model. The immiscibility of these mixtures with water prevents the use of monolayers of keratinocytes cultured in cell culture media. Following OECD 439 guidelines, a mixture was classified as non-irritating if the cell viability determined by MTT assay exceeds 50 %. An initial screening's objective with only one tissue sample per mixture was performed to identify the ammonium or phosphonium salts that yielded non-irritating mixtures. As Fig. S2 indicates, none of the mixtures with ammonium salts, with either short (C_4) or long (C_8) carbon chains, showed viability above 10 %. In contrast, mixtures with phosphonium salts, particularly those containing [P66614], showed promising results. Specifically, viability was 71 % in combination with monoolein and 80 % with tetradecan-1-ol. As anticipated, mixtures with carboxylic acid were found to be irritating (Radošević et al., 2015; Santos et al., 2018; Paiva et al., 2014), leading to the exclusion of fatty acids as HBD candidates. For [P6668]-based mixtures, viability consistently remained below 10 %; however, due to their similarity in carbon-length, these were retained as references for subsequent characterizations. Based on these initial findings, we decided to proceed with seven mixtures based on [P6668] or [P66614] as listed in Table 1.

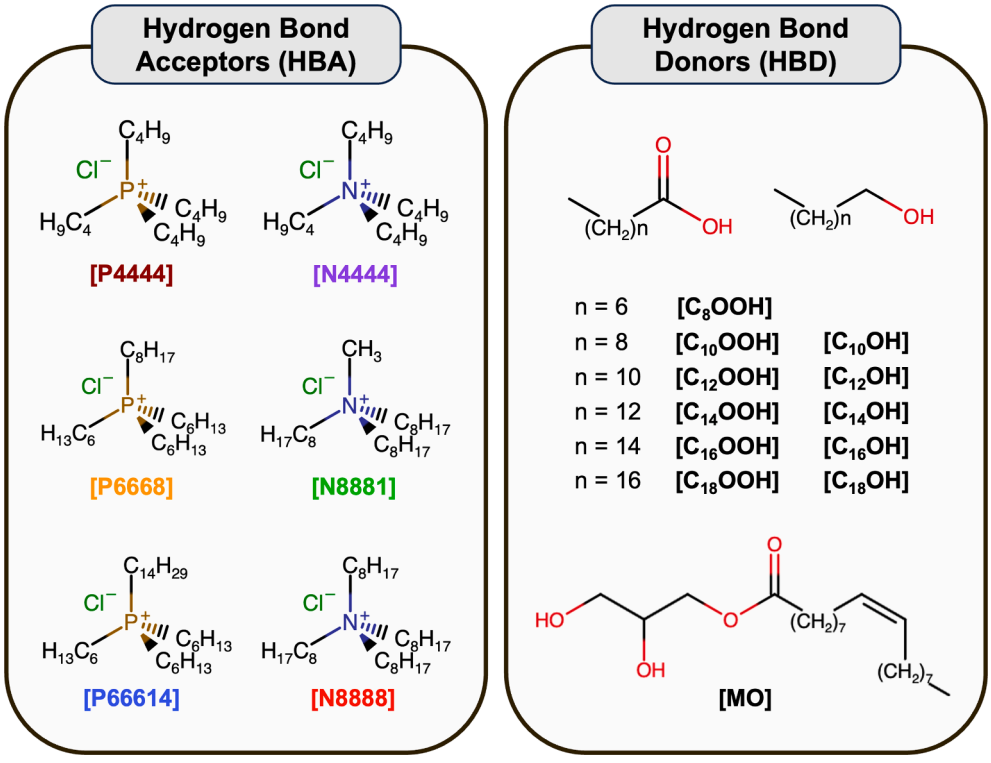

Fig. 1. Chemical structures of HBAs and HBDs used for mixtures preparation and their respective acronyms.

Considering the previously noted hygroscopic properties of ammonium and phosphonium salts (Dwamena, 2019; Naik et al., 2019), we employed Karl-Fischer titration to determine the water content of the prepared mixtures. Pure [P6668] and [P66614] salts had a humidity level of 0.24 % and 0.47 % respectively. Without any pre-drying step, the measured water content of all mixtures was consistently <0.25 %, thus confirming their hydrophobic nature.

3.2. Thermal properties

Differential Scanning Calorimetry (DSC) was used to determine the phase transition behavior of the mixtures and verify the melting temperature depression. We generated six phase diagrams for mixtures composed of phosphonium salts in combination with fatty alcohols (C_{12}, C_{14} and C_{16}) as shown in Fig. 2. The melting temperatures (T_m) were determined for each ratio with a step of 0.1. However, thermograms of mixtures based on [P6668] at ratios below 0.6 presented almost flat lines from −50 °C to 25 °C in the instrument's measurement range. Consecutively, as thermal events probably exceeded this range, low-temperature DSC was used to determine the melting temperatures of the 1:1 ratio and the glass transition temperatures (T_g) of the pure phosphonium salts. For mixtures based on [P66614], no significant negative deviations from ideality were observed and therefore these mixtures can neither be qualified as eutectic solvents nor deep eutectic solvents. Instead, they exhibit linearity to the extent that categorizing them as ideal solvents would be more appropriate, especially for [P66614][C_{16}OH]. This suggests that there is no hydrogen bond network coming into play within these mixtures. Because of the lack of information regarding [P6668] mixtures, drawing conclusions about the presence of a eutectic point proved to be more challenging. All the thermograms are presented in Fig. S3.

The low-temperature DSC curves for seven equimolar mixtures as well as those of the pure phosphonium salts were obtained at a scan rate of 5 °C·min^{-1}. Fig. 3 presents the corresponding thermograms with starting phase transition temperatures (T_g and T_m) indicated by arrows, which are also listed in Table 2. The heating profiles for both pure [P6668] and [P66614] showed a glass transition temperature at approximately −75 °C. This T_g remained present within all mixtures, but it was more difficult to detect as the low-temperature limit was approached, notably for [P6668][C_{12}OH]. Mixture melting points increased with increasing alcohol chain length, i.e., T_m of 1:1 [P66614]-based mixtures with [C_{12}OH], [C_{14}OH] and [C_{16}OH] are respectively: −71.2 °C, −67.7 °C and −64.8 °C. To avoid metastable phases (Rycerz, 2013), we carefully prepared the samples by heating and vortexing them, followed by repeated heating and cooling cycles. Despite these precautions, the thermal events observed were not sharp but rather spread over a wide temperature range. This spread often involved a sequence of melting-recrystallization-melting phenomenon. A similar pattern was noted in some of the pure alcohol samples, as shown in the thermograms of the starting materials in Fig. S4.

Upon mixing, the two transition events that are typically seen in pure monoolein were no longer present. The main transition event that usually occurs at 26.4 °C disappeared. Additionally, the smaller peak, often

Table 1
List of Hydrogen Bond Acceptors (HBAs) and Donors (HBDs) combinations, used for mixtures preparation, including molar ratios and water contents determined by Karl Fischer titration (N=1).

HBAs	HBDs	Molar ratios	H_2O [%]
[P6668]	[C_{12}OH]	1:1	0.22
[P6668]	[C_{14}OH]	1:1	0.21
[P6668]	[C_{16}OH]	1:1	0.16
[P66614]	[C_{12}OH]	1:1	0.22
[P66614]	[C_{14}OH]	1:1	0.22
[P66614]	[C_{16}OH]	1:1	0.16
[P66614]	[MO]	1:1	0.20

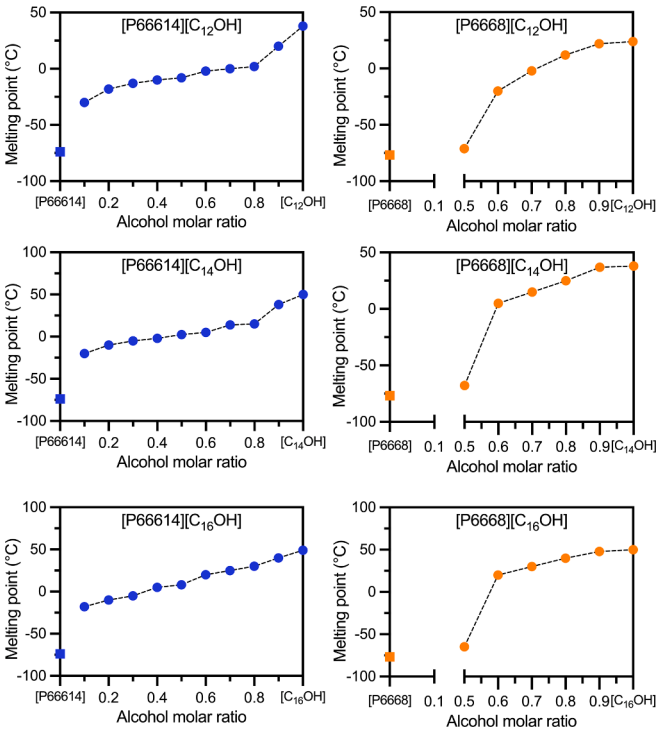

Fig. 2. Phase diagrams of six phosphonium/fatty alcohol mixtures. Melting and glass temperature transitions measured in single replicate are symbolized by circles (●) and squares (■), respectively.

observed around −10 °C and attributed to the crystallization of water trapped in the material (Réeff et al., 2013), appeared to have been eliminated due to the introduction of hydrophobic HBA. The absence of the main transition event within the studied temperature range indirectly suggests that there was a depression in the melting temperatures. Therefore, the [P66614][MO] mixture could very well present an eutectic V-shape solid–liquid phase diagram. It only exhibited a single transition, specifically a glass transition. While it is challenging to attribute this transition solely to [P66614] or to the combined effect of both components, it is reasonable to qualify [P66614][MO] as a LTTM mixture (Francisco et al., 2012). This assertion is further supported by the description of a very similar mixture in a patent (Patil and Bodige, 2016).

3.3. Thermal stability

Thermogravimetric Analysis (TGA) was employed to assess the thermal stability of various mixtures and their individual components. The TGA profiles, depicted in Fig. 4A, reveal that both pure phosphonium salts exhibited remarkably similar thermal degradation behaviors, starting at around 342 °C. This finding aligns with previous studies (Fraser and MacFarlane, 2009; Deferm et al., 2018), which reported degradation temperatures in the range of 330 to 350 °C. All the studied mixtures underwent two stages of degradation. The first degradation event (T_{d1}) is associated with the breakdown of the HBD, while the second (T_{d2}) corresponds to the degradation of the HBA. We observed that the energy required for the thermal degradation of pure alcohols increased in a manner directly proportional to their chain length (see dotted lines). This relationship exhibited a strong linear correlation (R^2 > 99 %), a trend that persisted even after the introduction of HBAs, as shown in Fig. S3. Further analysis, presented in Fig. 4B and Table 2, revealed that the starting degradation temperatures ($T_{d1,ONSET}$) of the alcohol mixtures were approximately 10 °C higher than those of the pure alcohols. This slight elevation in $T_{d1,ONSET}$, particularly suggests the possibility of minor interactions occurring within these mixtures,

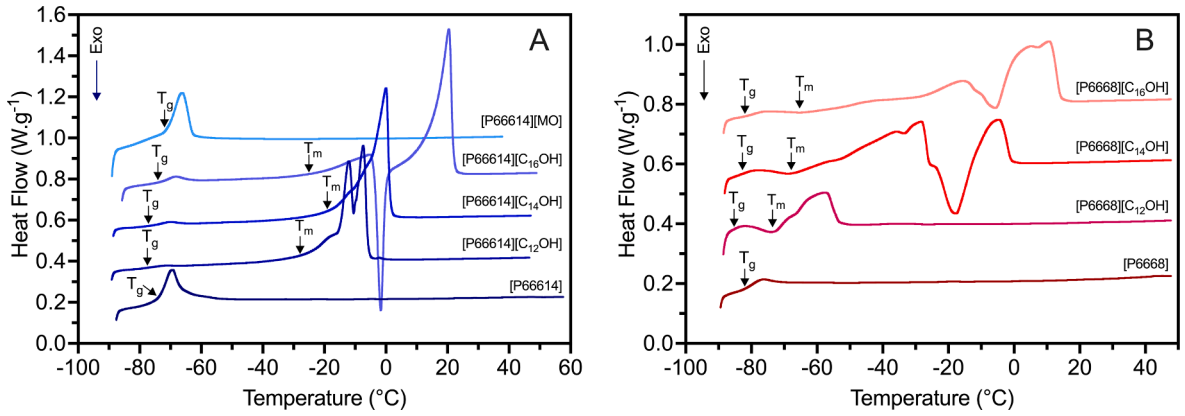

Fig. 3. DSC thermograms of [P66614]-based mixtures (A) and [P6668]-based mixtures (B), both in equimolar ratio with fatty alcohols (C_{12}, C_{14} and C_{16}) or [MO] as specified by acronyms.

Table 2
Glass transition (T_g), melting (T_m), and degradation (T_{d1}, $T_{d2\ and}$ $T_{d5\%}$) temperatures for the studied systems. $\Delta m_{100\ °C}$ represents the weight loss at 100 °C determined via TGA.

Mixtures	$T_{g\ ONSET}$ [°C]	$T_{m\ ONSET}$ [°C]	T_{d1} [°C]		T_{d2} [°C]		$T_{d\ 5\ \%}$ [°C]	$\Delta m_{100\ °C}$ [%]
			ONSET	END	ONSET	END		
[C_{12}OH]	—	22.1	120.4	152.5	—	—	88.1	9.5
[P6668][C_{12}OH]	n.d.	−73.0	132.5	188.6	342.7	384.2	129.5	1.8
[P66614[C_{12}OH]	−77.2	−27.9	132.3	191.6	343.6	384.8	128.8	1.8
[C_{14}OH]	—	35.3	137.1	172.7	—	—	112.4	2.1
[P6668][C_{14}OH]	n.d.	−67.7	151.3	206.6	342.6	383.9	144.4	1.4
[P66614][C_{14}OH]	−77.1	−18.7	151.3	207.7	343.6	385.0	141.7	1.8
[C_{16}OH]	—	48.7	160.2	194.3	—	—	137.9	0.1
[P6668][C_{16}OH]	− 81.9	−64.8	169.2	222.7	343.3	383.6	162.9	1.4
[P66614][C_{16}OH]	−73.9	−26.5	168.8	223.5	343.0	383.8	157.3	1.7
[MO]	—	26.4	220.1	n.d.	n.d.	393.5	212.2	0.2
[P66614][MO]	−71.0	—	272.0	n.d.	n.d.	382.0	197.3	1.3
[P6668]	−82.1	—	342.7	384.1	—	—	254.7	2.4
[P66614]	−73.9	—	341.8	382.8	—	—	196.7	2.3

n.d.: not determined.

despite their phase diagrams indicating ideal behavior. Similarly, minor interactions between [P66614] and [MO] were suspected, $T_{d1,ONSET}$ of this mixture increased by 52 °C, while the $T_{d2,END}$ decreased by 11 °C compared to the pure monoolein.

The evaluation of short-term stability was based on a combination of $T_{d1,ONSET}$ and $T_{d5\%}$, representing the temperature at which 5 % of the sample degraded. Typically, these two values show a strong correlation with each other: this is also what we observed here with $R^2 = 0.79$ (Fig. S4). Among all mixtures, [P66614][MO] demonstrated the highest stability, with a $T_{d5\%}$ value of 197.3 °C. This suggests that the inclusion of quaternary phosphoniums salts may slightly enhance the thermal stability of the alcohol-based mixtures.

We also evaluated the water content in both the starting materials and the mixtures using TGA. The weight loss observed at 100 °C, which we refer to as $\Delta m_{100°C}$, is reported in Table 2. These values are greater than those obtained from Karl Fischer titration, this discrepancy is probably due to the relative volatility of the fatty alcohols.

3.4. Liquid state organization

X-ray and neutron diffraction studies conducted on ILs and DESs have revealed the existence of nanoscale ordering, which could also reflect the presence of a hydrogen bond network within these liquids (Hardacre et al., 2010; Russina and Triolo, 2017; Song et al., 2012; Greaves et al., 2010; Triolo et al., 2012; Pott and Méléard, 2009; Hammond et al., 2016; Gontrani et al., 2009). These findings have consistently been supported by Molecular Dynamics Simulations (MDS), Empirical Potential Structure Refinement (EPSR), and Radial Distribution Functions (RDFs). The authors of these studies have also been able to assign intra- and intermolecular bonding contributions. In this study, we conducted small- and wide-angle X-ray scattering (SWAXS) experiments to question whether certain arrangements and hydrogen bonds existed in our mixtures. Furthermore, we aimed to examine how the length of the alkyl chains influenced the formation of a potential three-dimensional network.

Within the q-range we acquired, spanning from 0.019 $Å^{-1}$ to approximately 1.9 $Å^{-1}$, all samples including pure [P6668] and [P66614] showed two distinct peaks, one at around $q_1 \approx 0.4\ Å^{-1}$ and the other at $q_2 \approx 1.4\ Å^{-1}$ (Fig. 5A). The first correlation peak corresponded to the largest distance (d_1) and varied from 16.1 to 16.9 Å for [P6668] mixtures. For [P66614] mixtures, it ranged from 18.7 to 20.4 Å. Both phosphonium mixtures are showing an increase with the length of the alcohol alkyl chain (Fig. 5B).

The greater slope observed [P66614]-based mixtures compared to [P6668]-based mixtures can be attributed to the increased steric repulsion of the C_{14} chains in contrast to C_8. The 2nd correlation peak at $q_2 = 1.41 \pm 0.01\ Å^{-1}$, remained fixed across all samples and corresponds to a 4.46 Å distance.

We observed similar diffraction patterns to those that have been documented in the previously cited studies. In particular, we can compare our data to the case of [P66614][Cl] ionic liquid from Gontrani et al.'s work (Gontrani et al., 2009). The authors observed two diffraction peaks ($d_1 = 17.2$ Å; $d_2 = 4.5$ Å) at room temperature. Their findings suggest that the high-q peak corresponds to intermolecular structure correlations, while the low-q peak relates to structural heterogeneities, resulting in an overall sponge-like morphology. These conclusions are

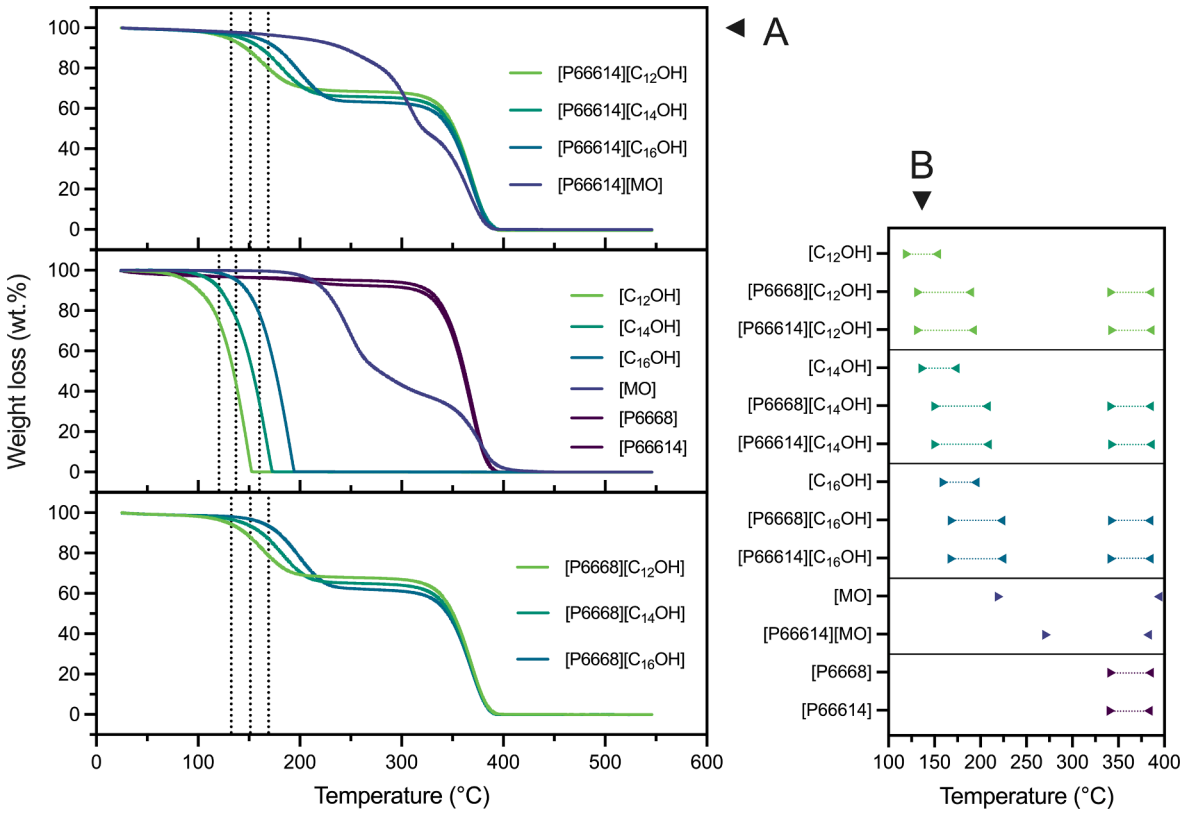

Fig. 4. Thermogravimetric curves from single replicates of mixtures in top and bottom frames and their individual components in the middle frame (A). Dotted lines indicate $T_{d1,ONSET}$ of alcohol-based mixtures and $T_{d2,END}$ of [MO]-based mixtures. Summary of the degradation ranges temperature for each sample, T_{ONSET} (▶) and T_{END} (◀) values of each event are represented (B).

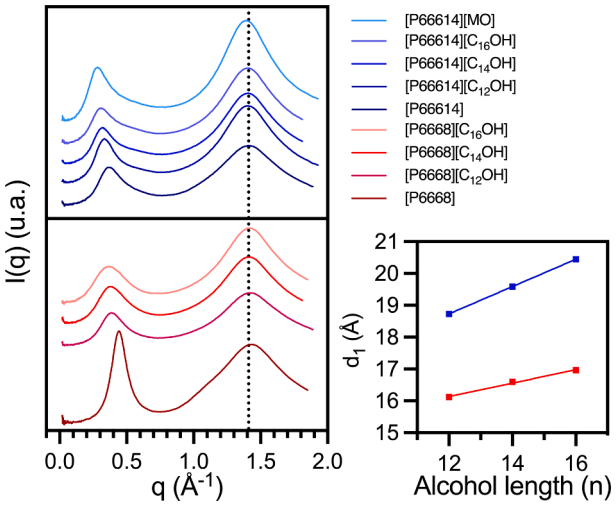

Fig. 5. Small- and wide-angle X-ray scattering profiles obtained for pure [P6668] and [P66614], as well as their respective mixtures, at 26 °C from single replicates (A). Low-q correlation distance (d_1) is plotted as a function of the alcohol chain length (n), revealing a close fit with $R^2 = 1$ for [P6668] mixtures and $R^2 = 0.995$ for [P66614] mixtures (B).

supported by other related. In our experiments, at 26 °C, the [P66614] liquid exhibited two correlation peaks, corresponding to $d_1 = 16.7$ Å and $d_2 = 4.5$ Å, which are close to their observations, when taking into account the temperature difference.

Considering the similar composition of our mixtures and their similar diffraction profiles, we can reasonably conclude that they also share a sponge-like structure. Nevertheless, this morphology was slightly affected by the addition of HBDs, as shown by the decrease in the low-q peak position. Typically, this peak is observed around 0.4 $Å^{-1}$, and has been shown to correlate with one component alkyl chain length across various series of ILs (Hardacre et al., 2010; Russina and Triolo, 2017; Song et al., 2012; Greaves et al., 2010; Pott and Méléard, 2009). The relationship between the low-q peak position (q_1) and the length of the alcohol indicates that this phenomenon is due to the expansion in the coordination lattice around phosphonium salts. However, SWAXS experiments are not sufficient to confirm the presence of a potential hydrogen bond network; this requires a thorough assessment of the radial distribution.

3.5. Polarity and hydrophobicity

Understanding the polarity and hydrophobicity of our mixtures would bring insights into their solvation capacity. Firstly, we assessed the polarity through the solvatochromism phenomenon (Reichardt, 1994), employing the Nile Red probe. Its solvation depends on the polarity of the surrounding medium, resulting in a shift in its maximum absorption wavelength ($\lambda_{max,NR}$). We measured this value across all binary mixtures, their starting components, and some standard solvents with established polarities, as displayed in Fig. 6A. Mixtures based on [P6668] were more polar than those based on [P66614], probably due to the shorter carbon chain. Monoolein was the HBD compound that offered the highest polarity, which could be supposed to be due to its high oxygen to carbon ratio compared to fatty alcohol HBDs. Overall polarity involves numerous constants and parameters such as dipole moment, dielectric constant, proticity, and others, making it challenging to quantify through empirical means. Nevertheless, we observed a notable correlation ($R^2 = 0.83$, Fig. S5) between $\lambda_{max,NR}$ and the dielectric constant of reference solvents (CRC Handbook of Chemistry and Physics; Lide, 2005). Considering the positions of our binary

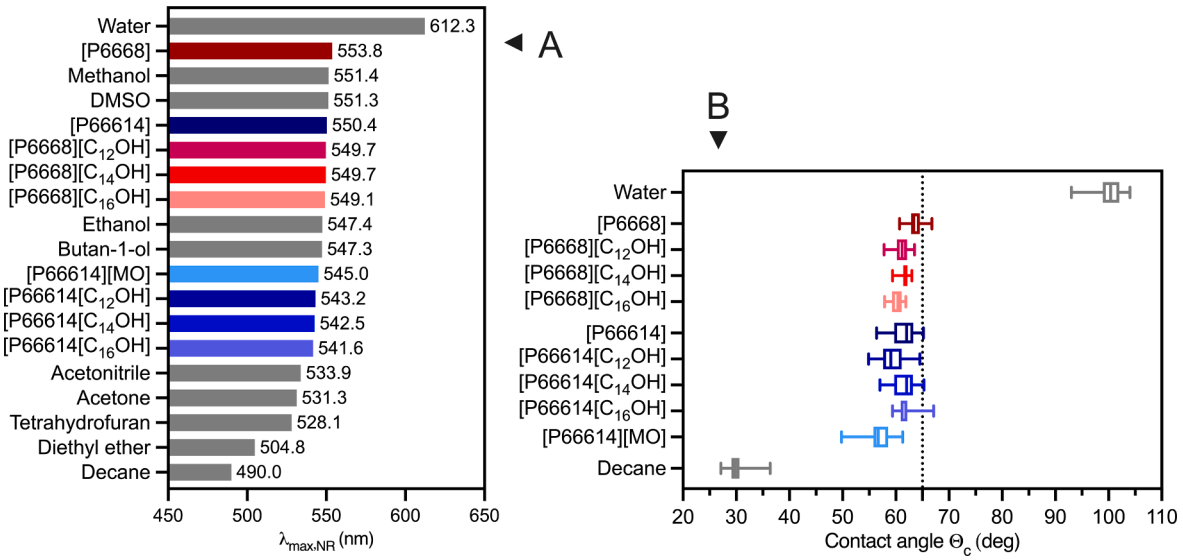

Fig. 6. Maximum wavelength absorption of the Nile Red probe within common solvent references (in grey) and studied systems (A) determined from absorption spectra measured in single replicates. Contact angle measurements (N = 10) on a Teflon surface for purified water, decane, and the studied systems (B).

mixtures, it appeared that they tended more toward the polar side, exhibiting a polarity close to DMSO, butan-1-ol, and acetonitrile.

We then assessed hydrophobicity using contact angle measurements on a smooth Teflon surface. By analyzing the shape of the droplets formed by our mixtures and two control solvents (purified water and decane), we estimated their hydrophobic or hydrophilic nature. Pure water, with a contact angle of 100.4°, served as a hydrophilic benchmark, while decane, at 29.8°, represented hydrophobicity. Those references set an intermediate boundary at around 65°. As shown by Fig. 6B, the average contact angle for all mixtures, except for [P66614][MO], was roughly 61 ± 1°. This positions them near this boundary, suggesting an amphiphilic character with a lean towards hydrophobicity. However, the [P66614][MO] mixture, with a contact angle of 56.7°, displayed a more pronounced hydrophobic character. In light of these results, and considering their water content (Table 1), we conclude that the prepared mixtures exhibit a polar, slightly hydrophobic, and non-hygroscopic nature, which greatly simplifies their storage and conservation.

3.6. Density

Density plays a fundamental role in solvent design and provides valuable insights into the internal interactions within a system. In our study, we measured the densities of all phosphonium mixtures across a temperature range of 25–50 °C. As depicted in Fig. 7A, the mixtures containing fatty alcohols showed a density of approximately 0.875 g·cm^{-3} at 25 °C. In contrast, the [P66614][MO] mixture had a notably higher density of 0.915 g·cm^{-3} at the same temperature. While the densities of fatty alcohols (around 0.82 g·cm^{-3}) and monoolein (about 0.94 g·cm^{-3} at 35 °C) were not measured in this study due to their solid state, the densities of the mixtures appear to be close to the average of these two initial constituents.

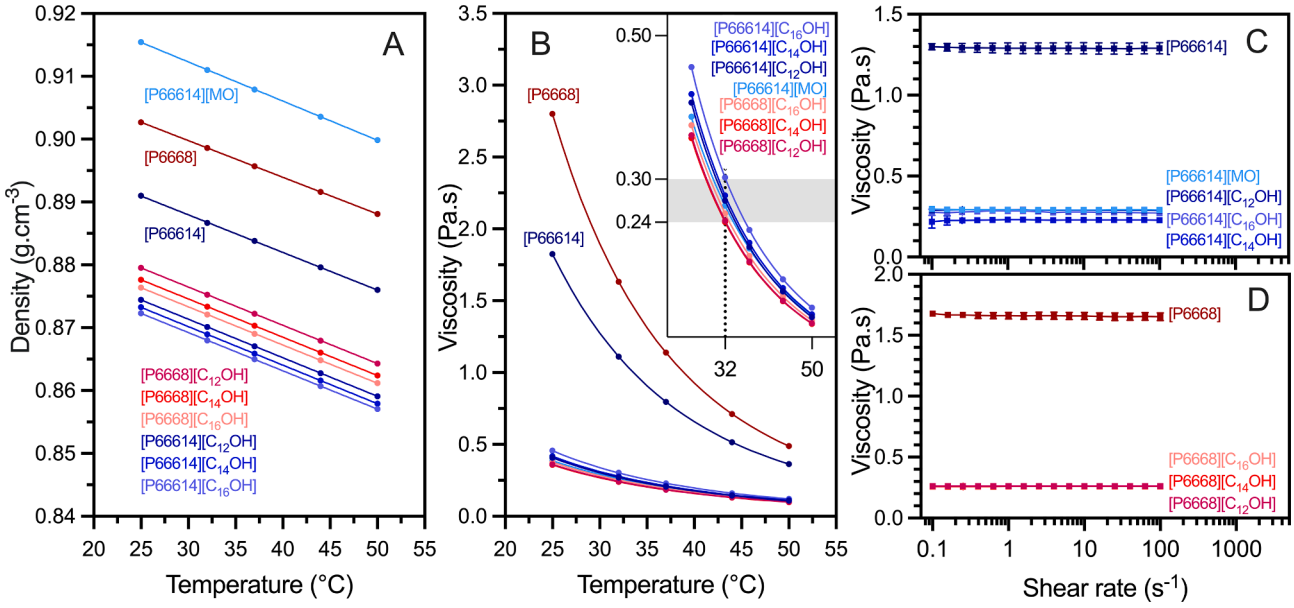

Fig. 7. Density (A) and dynamic viscosity (B) values (N = 1 for both) of the studied mixtures, as well as those of the pure phosphonium salts, as a function of temperature. Viscosity values from at least 3 replicates at 32 °C depending on the shear rate for the [P66614]-based mixture (C) and the [P6668]-based mixture (D). Error bars represent standard deviation relative to the mean values.

Previous research has shown very different density values for ammonium or phosphonium-based HDESs, ranging from lighter (Florindo et al., 2019) than water (around 0.9 g·cm^{-3}) to significantly denser (Wazeer et al., 2021) (around 1.20 g·cm^{-3}). Some studies, such as one by Abbott et al. (2007), suggested that hydrogen bondings within DESs can increase the mixture's density compared to its individual components due to a decrease in the average hole radius. Unfortunately, this theory did not seem to apply to our mixtures. Nevertheless, the densities we observed which differed significantly from that of water ($\rho \neq 1 \pm 0.05$) (Van Osch et al., 2019), make them ideal for applications such as liquid–liquid extraction.

We also noted that the density decreased with an increase in the length of the HBD alkyl chains, a trend consistent with observations in HDESs containing alkyl diols (Yusof et al., 2014) or carboxylic acids (Florindo et al., 2018). Additionally, the [P6668] mixtures were generally denser than the [P66614] mixtures when combined with the same HBD, a phenomenon also reported in ammonium salt-based ILs (Pott and Méléard, 2009). As expected, all our samples showed a predictable linear decrease in density with rising temperature, decreasing by approximately 0.00607 ± 0.00011 g·cm^{-3} for every 10 °C increase in temperature. For more detailed statistical analysis, such as fitting parameters, R2 values, and the Average Absolute Deviation (%AAD), refer to Table S2.

3.7. Viscosity and rheological behavior

Viscosity and rheological behavior are essential characteristics in terms of skin application. Topical creams are usually non-Newtonian, shear-thinning materials, meaning that the more they are spread by skin-on-skin friction, the more their viscosity decreases. For comparison, Leshcutan®, which is the commercial 15 % paromomycin topical treatment, is formulated with white soft paraffin (WSP) (El-On et al., 2007), which is a common ingredient to produce ointments in the pharmaceutical industry. At 30 °C and low shear rate, WSP has a dynamic viscosity ranging from 0.5 to 1.5 Pa.s depending on its origin and its composition (Barry and Grace, 1970).

At skin temperature (32 °C), the prepared mixtures exhibited a dynamic viscosity ranging from 0.24 to 0.30 Pa.s, as shown in Fig. 7B. These values are considered suitable for skin application. With increasing temperature, the viscosity decreased, and our calculations indicate that this trend aligns more closely with the Vogel-Fulcher-Tammann (VFT) law than the Arrhenius law (Table S3). As for the density measurements, the length of fatty alcohol chains affects the viscosity of the mixture, with longer chains resulting in higher viscosity. However, this effect is relatively subtle, as it was not consistently observed in rheological measurements (Fig. 7C).

For topical application, it is important that the initial viscosity is relatively high to maintain a certain consistency before spreading. However, the crucial factor is that the substance can be easily spread on the skin. Unfortunately, rheological measurements at 32 °C reveal that the prepared mixtures exhibited a Newtonian behavior (Fig. 7C and D). This means that their viscosity remains constant, regardless of penetration movements.

3.8. In-vitro irritation assessment

We assessed the irritation potential of seven mixtures using an epidermal tissue model and the MTT assay. This evaluation was more comprehensive than our initial rapid irritation screening. For a more thorough comparison, we included pure salts and a broader range of alcohols and the experiment was carried out on tissue samples. Additionally, to better understand the impact of both components, we tested two specific volumes of [P66614]: 20.8 µL and 18.3 µL. These volumes correspond to the amounts found in 30 µL of the [P66614][C_{14}OH] and [P66614][MO] mixtures, respectively. Our goal was to determine if the observed high viability was due to the addition of the HBDs or simply due to the reduced concentration of [P66614].

The results for the [P66614][C_{14}OH] and [P66614][MO] mixtures, presented in Fig. 8, were consistent with the initial screening, confirming the reliability of our experiments. The mixture containing monoolein particularly stood out, showing excellent repeatability and the highest cell viability at 68.8 ± 1.9 %. We also found that varying the carbon chain length of alcohols did not significantly correlate with the irritant potential of the mixtures. Interestingly, the inclusion of any HBDs with [P66614] reduced irritation. When pure [P66614] was applied in reduced volumes, it exhibited very low viability (<10 %), emphasizing the significant benefit of both HBDs ([C_{14}OH] and [MO]) in reducing irritability.

3.9. Histology

To assess potential adverse effects on skin health and functionality, staining and immunofluorescent labelling were conducted on a 3D epidermal tissue model incorporating both keratinocytes and fibroblasts. Of all the mixtures tested, [P66614][MO] not only showed the highest viability but also exhibited signs of eutectic behavior, leading to its selection. To provide context, DPBS was used as a negative control with no expected impact, while a mixture of choline chloride and malic acid (1:1), known to be irritant, acted as the positive control to gauge potential negative effects.

Firstly, epidermal thickness was measured after H&E staining to assess potential cellular under- or overproliferation in response to the applied mixtures (Fig. 9). For the DPBS negative control, the epidermis measured 73 ± 15 µm. For the positive control, a significant reduction to 54 ± 8 µm was noted, whereas the [P66614][MO] mixture showed no significant change, maintaining a thickness of 77 ± 8 µm. Next, we evaluated Ki67, a marker for cellular proliferation located predominantly in the stratum basale of the skin. Ki67 levels in the [P66614][MO] treated samples were comparable to those in the negative control (around 23 %). Furthermore, the TUNEL assay, used to detect apoptotic cells by identifying fragmented DNA, also did not exhibit any significant increase.

Our focus then shifted to tight junction proteins. Within the stratum

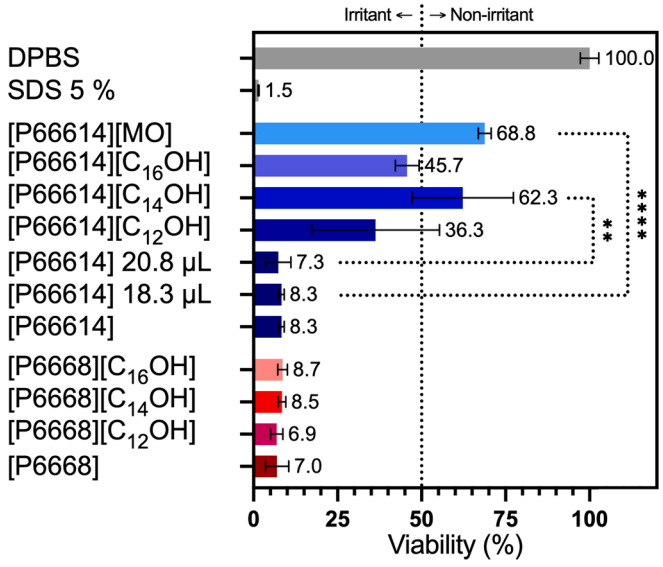

Fig. 8. Cell viability (%) of the EpiDermTM epidermal tissue model was measured using the MTT assay (N=3) with a 30 µL deposit for each sample, except for two [P66614] samples with 18.3 µL and 20.8 µL, as specified in the legend. DPBS was used as the negative control and SDS 5 % as the positive control. Error bars represent standard deviations relative to the mean values. p-value keys: ** ≤ 0.01; **** ≤ 0.0001.

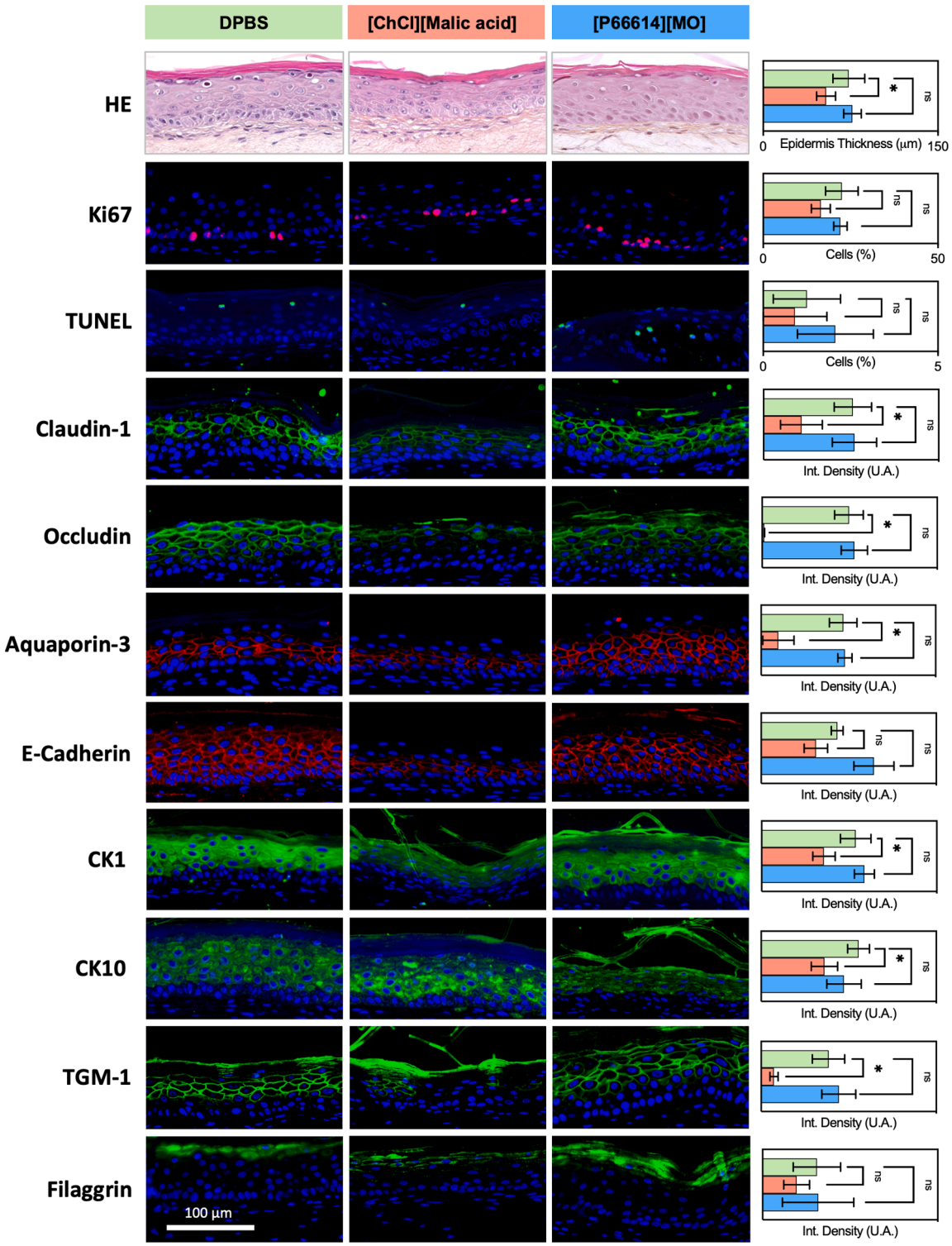

Fig. 9. Staining and immunofluorescence labelling of EpidermFT^{TM} tissue sections with antibodies to various epithelial markers after exposition to [P66614][MO] mixture (blue). DPBS was used as negative control (green) and [ChCl][Malic acid] was used as positive control (red). Repeatability was carried out on a single biological tissue (N=1), which was analyzed in 3 different sections to avoid a possible local effect and at least 5 images were extracted from each of these sections. Error bars represent standard deviations relative to the mean values. p-value keys: ns = not significant; * = $0.01 \leq p < 0.05$; ** = $0.001 \leq p < 0.01$.

granulosum layers, we specifically localized and quantified claudin-1 and occludin, both crucial for maintaining cell junction tightness. Additionally, aquaporin-3 and E-cadherin proteins contribute similarly to regulating water balance and skin elasticity but are widely distributed across the skin, except within the stratum corneum layers. While the malic acid-based mixture significantly reduced most of these proteins, the [P66614][MO] mixture did not induce any notable changes compared to the negative control.

We also examined two fibrous proteins: cytokeratins (CK1 and CK10), vital for mechanical support across all suprabasal layers. Their presence and quantity remained unchanged after treatment with the [P66614][MO] mixture. Similarly situated in suprabasal layers, the

transglutaminase 1 (TGM1) enzyme is essential for synthesizing cross-links between proteins and maintaining the skin barrier. This protein remained unaffected by the mixture, showing no significant under- or overexpression compared to the negative control. Filaggrin, exclusively located in the stratum corneum, is formed through keratinization process, and usually remains bound to keratin. It plays a crucial role in maintaining homeostasis. The quantity of filaggrin remained consistent across all three treatments. Ultimately, the examination of these crucial skin proteins indicates that the 3D epidermal tissue model was not significantly affected after exposure to the [P66614][MO] mixture in comparison with the two controls.

3.10. Solubility of Amphotericin B (AmB)

Amphotericin B (AmB) is an amphiphilic molecule characterized by a hydrophilic segment of polyols and a hydrophobic portion of polyenes (Fig. 10A). Furthermore, AmB demonstrates amphoteric characteristics due to the presence of an amine group (pKa 8.12) and a carboxyl group (pKa 3.72). Therefore, AmB exhibits poor solubility in water and is only soluble in specific organic solvents, such as methanol and DMSO. Consequently, the incorporation of this active substance into pharmaceutical formulations is challenging.

In this study, we used HPLC quantification to measure the solubility of amphotericin B in reference solvents, pure phosphoniums, and the prepared mixtures (Fig. 10B). The measured concentration of AmB in DMSO was 43.1 mg·mL^{-1}, while it was only 0.005 mg·mL^{-1} in pure water. Notably, the solubility in [P66614] was approximately 0.79 mg·mL^{-1} exceeding that in pure [P6668], which was 0.48 mg·mL^{-1}. A similar trend was observed in the related mixtures, with [P6668]-based mixtures exhibiting lower solubility (0.35–0.44 mg·mL^{-1}) compared to [P66614]-based mixtures (0.50–0.81 mg·mL^{-1}).

Our findings align with the anticipated solubility from literature reports, which indicate AmB's insolubility in pure water (<0.001 mg·mL^{-1} (Torrado et al., 2008) and its solubility in DMSO (30–40 mg·mL^{-1} (Waugh, 2007). The solubilization and quantification processes may account for the slight deviation in our results. The difference in solubility between [P6668] and [P66614] mixtures can be attributed

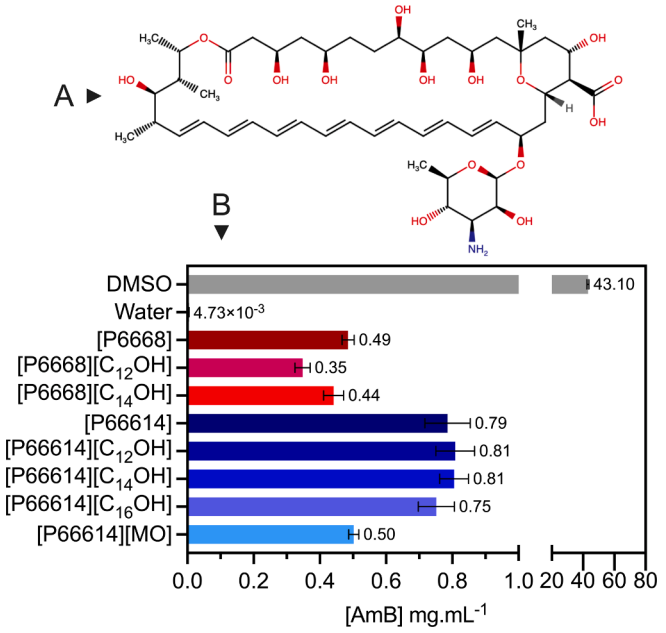

Fig. 10. Amphotericin B molecular structure (A) and its solubility quantifications (N = 3) in reference solvents (pure water and DMSO), pure phosphoniums and the prepared mixtures (B). Error bars represent standard deviations relative to the mean values.

to the latter's slightly more pronounced hydrophobic character, whereas the alcohol chain length does not seem to significantly impact solubility. In the context of topical formulation, the [P66614][C_{14}OH] mixture, for instance, can afford a mass concentration of approximately 0.1 % of amphotericin B.

3.11. Evaluation of AmB aggregation state

Owing to its amphiphilic nature, Amphotericin B (AmB) can self-aggregate depending on the medium, exhibiting various forms including monomers, soluble oligomers, and insoluble aggregates (Espada et al., 2008; Gaboriau et al., 1997; Silva, 2017). The drug aggregation state of AmB plays an important role in drug toxicity (Espada et al., 2008; Faustino and Pinheiro, 2020). The monomeric form is of particular interest due to its selective targeting of the cell membranes of fungi and parasites, which are rich in ergosterol, as opposed to the cell membranes of mammals, which have cholesterol instead. On the other hand, when self-associated into oligomers, the drug can also bind to cholesterol and generate toxic effects (Golenser and Domb, 2006; Grudzinski et al., 2016; Huang et al., 2002). Insoluble aggregates are believed to act as reservoirs, releasing monomers into the surrounding medium (Chéron et al., 2003). Spectroscopic analysis provides valuable insights into AmB's molecular associations, with the heptaene chain serving as a distinguishable feature in both UV–visible and circular dichroism (CD) spectroscopy. The latter is particularly valuable for discerning different forms of AmB organization.

We evaluated the aggregation state of AmB in various solvents, including pure water, a 1:1 DMSO:MeOH mixture, and our specific samples. UV–Vis spectroscopy revealed that AmB in pure water displayed a broad absorption band around 333 nm, indicative of the oligomeric state, whereas the monomeric state, present in DMSO:MeOH mixture, exhibited three major absorption bands at 367, 387, and 410 nm (Fig. 11A and B). [P66614]-based mixtures displayed characteristic bands of the monomeric state. Circular dichroism analysis (Fig. 11C and D) also supported these findings, with AmB in pure water exhibiting a dichroic doublet centered at 340 nm, indicating its self-aggregated state. Notably, DMSO:MeOH and [P66614]-based mixtures exhibited similar spectral characteristics.

The results from the reference solvents align with existing literature (Espada et al., 2008; Jameson and Dzyuba, 2013), confirming the monomeric state of AmB in the analyzed mixtures, supported by both electronic spectroscopy and circular dichroism. The same conclusion was drawn from the results of [P6668]-based mixtures, available in Fig. S8.

3.12. Irritation assessment of AmB formulations

Based on the irritation results and considering the physicochemical and solubility data, we selected two promising formulations: [P66614][C_{14}OH] and [P66614][MO]. Subsequently, the study was focused exclusively on these mixtures. The next goal was to determine the potential impact of AmB on keratinocyte viability. As illustrated in Fig. 12, The introduction of AmB at its maximum solubility significantly contributed to increased cell death for both mixtures. However, in the case of the [P66614][C_{14}OH] formulated at 0.4 mg·mL^{-1} of AmB, the observed reduction in viability did not significantly differ from the corresponding mixture without AmB. Although the AmB monomeric state was observed in these mixtures, the cell viability was still directly linked to AmB concentration. Hence, a concentration at half the maximum solubility would be optimal.

3.13. Evaluation of transcutaneous passage

Leishmania parasites primarily reside within macrophages located in the dermis. Achieving effective topical treatment for this disease requires penetration and delivery of the active substance to this dermal layer. To evaluate the potential for our formulations to carry out this

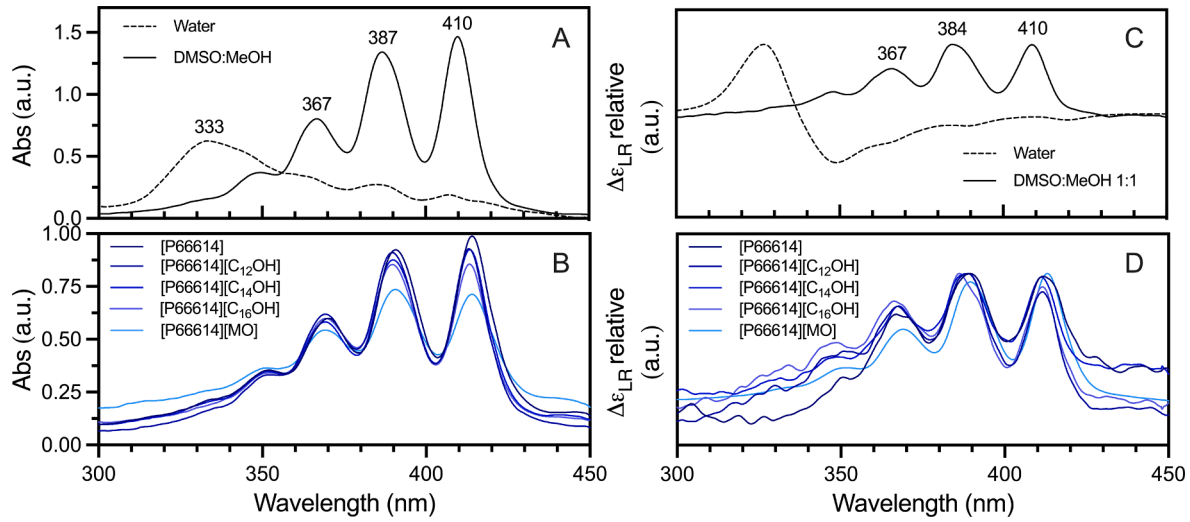

Fig. 11. Electronic absorption spectra (A and B) and circular dichroism (C and D) of reference solvents (pure water and DMSO:MeOH 1:1 v/v) and [P66614]-based mixtures containing AmB. All measurements were performed on single replicates.

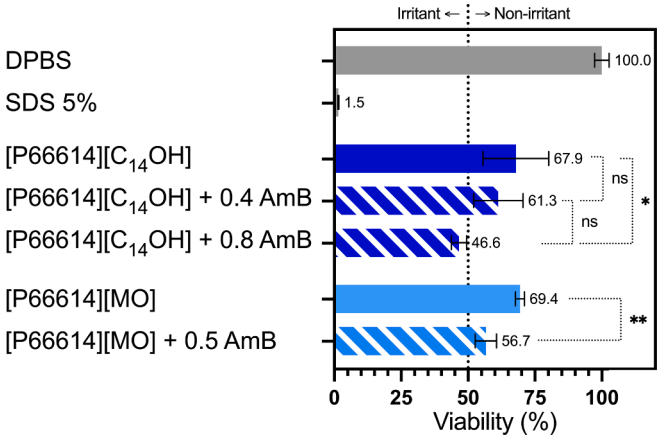

Fig. 12. Cell viability (%) of epidermal tissue model EpiDerm™ assessed by MTT test (N = 3). The crosshatched bars represent formulations containing a certain concentration of AmB (mg·mL^{-1}) specified in the legend. DPBS was used as a negative control and SDS 5 % as a positive control. Error bars represent standard deviations relative to the mean values. p-value keys: ns = not significant; * = 0.01 ≤ p < 0.05; ** = 0.001 ≤ p < 0.01.

type of delivery, a penetration study was conducted on pig ear skin using Franz cells. The study included assessment of [P66614][C14OH] and [P66614][MO] mixtures, which contained the maximum solubilized amounts of AmB, i.e. 0.8 and 0.5 mg·mL^{-1} of AmB respectively.

The experiment was conducted at 32 °C over a period of 4 days. Twelve solutions designed for the receptor compartment were tested to ensure their capability to dissolve all of the AmB, assuming it passes through the skin, as depicted in Table S4. The only solution that completely solubilized AmB was composed of DPBS (without divalent ions) with 1 % (w/v) sodium dodecyl sulfate (SDS). Considering the strong irritant nature of SDS, a preliminary test was conducted to assess its effect on the integrity of the skin from the receptor tank.

As a impermeability control, a concentrated 25 mg·mL^{-1} solution of fluorescein isothiocyanate labeled dextran 4400 (FITC-Dextran), which is too large to pass through intact skin, was used. The quantity of FITC-Dextran was analyzed using UV–vis absorbance spectroscopy in the six receptor tanks, with three containing SLS and three without. The results revealed that both receptor media contained less than 2 µg·mL^{-1} of FITC-Dextran after 4 days, indicating a passage rate of 0.1 %. Consequently, SLS did not demonstrate a corrosive effect on the hypodermis, indicating its suitability for AmB solubilization. The impermeability of the experimental system was also confirmed by this control.

The main penetration test involved applying 88 µL (i.e. 50 µL·cm^{-2}) of [P66614][C_{14}OH] and [P66614][MO] (N = 3 each) containing the maximum tolerated amount of AmB. The previously selected and validated receptor solution was used. After 4 days, the concentration of AmB in the medium was measured via UV–vis spectrometry, revealing that none had crossed the skin. The AmB either stayed on the skin surface without penetrating or became entrapped within the skin layers. The latter scenario would be particularly desirable as it could allow a localized action without systemic absorption, thereby potentially avoiding toxic effects.

4. Conclusion

In this study, we explored HDESs and other hydrophobic mixtures for their potential use as excipients for skin applications. Our findings highlighted that mixtures based on [P66614] showed promising tolerance as evidenced from the irritation tests. While thermal and structural analyses did not identify a eutectic point in alcohol-based mixtures, they suggested the presence of a sponge-like structure. However, a eutectic behavior within the [P66614][MO] mixture seems likely but requires further confirmation. Comprehensive physicochemical characterization of these mixtures indicated their potential for a wide range of applications. Their polarity and lipophilicity appeared particularly suitable for dissolving AmB. Histological examination on a 3D skin tissue model revealed no adverse effects from the [P66614][MO] mixture. Moreover, the formulation showed no signs of transcutaneous passage in pig ear skin, predicting a strictly localized action. [P66614][MO] and [P66614][C_{14}OH] have shown promising properties, in particular their capability to dissolve AmB in its monomeric form, making them worthy of further investigation as a topical treatment for CL.

CRediT authorship contribution statement

Luc Augis: Writing – review & editing, Writing – original draft, Visualization, Methodology, Investigation, Formal analysis. **Cảnh Hưng Nguyễn:** Writing – review & editing, Investigation, Formal analysis. **Cécile Ciseran:** Investigation. **András Wacha:** Writing – review & editing, Investigation. **Françoise Mercier-Nomé:** Writing – review & editing, Visualization, Methodology, Investigation. **Séverine Domenichini:** Writing – review & editing, Software, Methodology, Investigation. **Christina Sizun:** Writing – review & editing, Investigation.

Sophie Fourmentin: Writing – review & editing, Investigation, Formal analysis. **François-Xavier Legrand:** Writing – review & editing, Supervision, Project administration, Methodology, Funding acquisition, Formal analysis, Conceptualization.

Declaration of competing interest

The authors declare the following financial interests/personal relationships which may be considered as potential competing interests: François-Xavier LEGRAND reports financial support was provided by French National Research Agency. Andras WACHA reports financial support was provided by Hungarian National Research, Development and Innovation Office. Andraas WACHA reports financial support was provided by Hungarian Academy of Sciences. If there are other authors, they declare that they have no known competing financial interests or personal relationships that could have appeared to influence the work reported in this paper.

Data availability

Data will be made available on request.

Acknowledgements

This work benefited from the full support of the project ParasiDES ANR-19-CE18-0027 of the French National Research Agency (ANR). Dr Luc AUGIS acknowledges the French National Research Agency for his doctoral scholarship. Dr Andras WACHA acknowledges the support of the János Bolyai Research Fellowship of the Hungarian Academy of Sciences and the support from the Hungarian National Research, Development and Innovation Office (NKFIH, grants FK146081, 2020-1-1-2-PIACIKFI_2020-00021, TKP2021-EGA-13). Dr Sandrine COJEAN is acknowledged for preliminary *in-vitro* efficacy assays on *L. major*. The authors would like to thank Mr. Frédéric HOPPENOT and Mr. Sébastien LAHALLE from TA Instruments (Guyancourt, France) for TGA and low-temperature DSC analysis. The authors thank the PHIC platform and Mr. Morgan OCIMEK for his assistance. We acknowledge Dr Gillian BARRATT for her careful reading. Abstract figure was partly generated using Servier Medical Art, provided by Servier, licensed under a Creative Commons Attribution 3.0 unported license.

Appendix A. Supplementary data

Supplementary data to this article can be found online at https://doi.org/10.1016/j.ijpharm.2024.124486.

References

Abbott, A.P., Capper, G., Davies, D.L., Rasheed, R.K., Tambyrajah, V., 2003. Novel solvent properties of choline chloride/urea mixtures. Chem. Commun. 1, 70–71. https://doi.org/10.1039/b210714g.

Abbott, A.P., Boothby, D., Capper, G., Davies, D.L., Rasheed, R.K., 2004. Deep eutectic solvents formed between choline chloride and carboxylic acids: versatile alternatives to ionic liquids. J. Am. Chem. Soc. 126 (29), 9142–9147. https://doi.org/10.1021/ja048266j.

Abbott, A.P., Barron, J.C., Ryder, K.S., Wilson, D., 2007. Eutectic-based ionic liquids with metal-containing anions and cations. Chem. - Eur. J. 13 (22), 6495–6501. https://doi.org/10.1002/chem.200601738.

Abranches, D.O., Coutinho, J.A.P., 2023. Everything you wanted to know about deep eutectic solvents but were afraid to be told. Annu. Rev. Chem. Biomol. Eng. 14 (1), 141–163. https://doi.org/10.1146/annurev-chembioeng-101121-085323.

AlOmar, M.K., Alsaadi, M.A., Hayyan, M., Akib, S., Hashim, M.A., 2016. Functionalization of CNTs surface with phosphonuim based deep eutectic solvents for arsenic removal from water. Appl. Surf. Sci. 389, 216–226. https://doi.org/10.1016/j.apsusc.2016.07.079.

AlOmar, M.K., Alsaadi, M.A., Hayyan, M., Akib, S., Ibrahim, M., Hashim, M.A., 2017. Allyl triphenyl phosphonium bromide based DES-functionalized carbon nanotubes for the removal of mercury from water. Chemosphere 167, 44–52. https://doi.org/10.1016/j.chemosphere.2016.09.133.

Barry, B.W., Grace, A.J., 1970. Grade variation in the rheology of white soft paraffin B.P. J. Pharm. Pharmacol. 22, 147S–S156. https://doi.org/10.1111/j.2042-7158.1970.tb08594.x.

Berman, J.D., 1997. Human leishmaniasis: clinical, diagnostic, and chemotherapeutic developments in the last 10 years. Clin. Infect. Dis. 24 (4), 684–703. https://doi.org/10.1093/clind/24.4.684.

Cao, J., Yang, M., Cao, F., Wang, J., Su, E., 2017. Well-designed hydrophobic deep eutectic solvents as green and efficient media for the extraction of artemisinin from artemisia annua leaves. ACS Sustain. Chem. Eng. 5 (4), 3270–3278. https://doi.org/10.1021/acssuschemeng.6b03092.

Chabasse, D., Pihet, M., 2014. Les onychomycoses à moisissures. J. Mycol. Méd. 24 (4), 261–268. https://doi.org/10.1016/j.mycmed.2014.10.005.

Chen, C.-C., Huang, Y.-H., Hung, S.-M., Chen, C., Lin, C.-W., Yang, H.-H., 2021. Hydrophobic deep eutectic solvents as attractive media for low-concentration hydrophobic VOC capture. Chem. Eng. J. 424, 130420 https://doi.org/10.1016/j.cej.2021.130420.

Chéron, M., Petit, C., Bolard, J., Gaboriau, F., 2003. Heat-induced reformulation of amphotericin b-deoxycholate favours drug uptake by the macrophage-like cell line J774. J. Antimicrob. Chemother. 52 (6), 904–910. https://doi.org/10.1093/jac/dkg455.

Comité OMS d'experts de la lutte contre les leishmaniosis, 2011. Organisation mondiale de la Santé. La lutte contre les leishmanioses. Control Leishmaniases Rep. Meet. WHO Expert Commitee Control Leishmaniases Geneva 22-26 March 2010.

CRC Handbook of Chemistry and Physics Lide, D. R. (Ed.), 2005.

Cruz, H., Jordão, N., Branco, L.C., 2017. Deep Eutectic Solvents (DESs) as low-cost and electrolytes for electrochromic devices. Green Chem. 19 (7), 1653–1658. https://doi.org/10.1039/C7GC00347A.

Deep Eutectic Solvents for Medicine, Gas Solubilization and Extraction of Natural Substances, 2021. Fourmentin, S., Costa Gomes, M., Lichtfouse, E., Eds.; Environmental Chemistry for a Sustainable World; Springer International Publishing: Cham, vol. 56. https://doi.org/10.1007/978-3-030-53069-3.

Deferm, C., Van Den Bossche, A., Luyten, J., Oosterhof, H., Fransaer, J., Binnemans, K., 2018. Thermal stability of trihexyl(tetradecyl)phosphonium chloride. Phys. Chem. Chem. Phys. 20 (4), 2444–2456. https://doi.org/10.1039/C7CP08556G.

Dietz, C.H.J.T., Creemers, J.T., Meuleman, M.A., Held, C., Sadowski, G., Van Sint Annaland, M., Gallucci, F., Kroon, M.C., 2019. Determination of the total vapor pressure of hydrophobic deep eutectic solvents: experiments and perturbed-chain statistical associating fluid theory modeling. ACS Sustain. Chem. Eng. 7 (4), 4047–4057. https://doi.org/10.1021/acssuschemeng.8b05449.

Diogo, J.C.F., Caetano, F.J.P., Fareleira, J.M.N.A., Wakeham, W.A., 2014. Viscosity measurements on ionic liquids: a cautionary tale. Int. J. Thermophys. 35 (9–10), 1615–1635. https://doi.org/10.1007/s10765-013-1487-y.

Du, C., Zhao, B., Chen, X.-B., Birbilis, N., Yang, H., 2016. Effect of water presence on choline chloride-2urea ionic liquid and coating platings from the hydrated ionic liquid. Sci. Rep. 6 (1), 29225. https://doi.org/10.1038/srep29225.

Dwamena, A., 2019. Recent advances in hydrophobic deep eutectic solvents for extraction. Separations 6 (1), 9. https://doi.org/10.3390/separations6010009.

Dwamena, A.K., Raynie, D.E., 2020. Solvatochromic parameters of deep eutectic solvents: effect of different carboxylic acids as hydrogen bond donor. J. Chem. Eng. Data 65 (2), 640–646. https://doi.org/10.1021/acs.jced.9b00872.

EI-On, J., Jacobs, G.P., Weinrauch, L., 1988. Topical chemotherapy of cutaneous leishmaniasis. Parasitol. Today 4 (3), 76–81. https://doi.org/10.1016/0169-4758(88)90200-1.

El-On, J., Bazarsky, E., Sneir, R., 2007. Leishmania Major. In Vitro and in Vivo Anti-Leishmanial Activity of Paromomycin Ointment (Leshcutan) Combined with the Immunomodulator Imiquimod. Exp. Parasitol. 116 (2), 156–162. https://doi.org/10.1016/j.exppara.2006.12.004.

El-Safi, S.H., Murphy, A.G., Bryceson, A.D.M., Neal, R.A., 1990. A double-blind clinical trial of the treatment of cutaneous leishmaniasis with paromomycin ointment. Trans. R. Soc. Trop. Med. Hyg. 84 (5), 690–691. https://doi.org/10.1016/0035-9203(90)90146-6.

Espada, R., Valdespina, S., Alfonso, C., Rivas, G., Ballesteros, M.P., Torrado, J.J., 2008. Effect of aggregation state on the toxicity of different amphotericin b preparations. Int. J. Pharm. 361 (1–2), 64–69. https://doi.org/10.1016/j.ijpharm.2008.05.013.

Faustino, C., Pinheiro, L., 2020. Lipid systems for the delivery of amphotericin b in antifungal therapy. Pharmaceutics 12 (1), 29. https://doi.org/10.3390/pharmaceutics12010029.

Feuilhade De Chauvin, M., 2014. Traitement des onychomycoses. J. Mycol. Méd. 24 (4), 296–302. https://doi.org/10.1016/j.mycmed.2014.10.009.

Florindo, C., Oliveira, F.S., Rebelo, L.P.N., Fernandes, A.M., Marrucho, I.M., 2014. Insights into the synthesis and properties of deep eutectic solvents based on cholinium chloride and carboxylic acids. ACS Sust. Chem. Eng. 2 (10), 2416–2425. https://doi.org/10.1021/sc500439w.

Florindo, C., Branco, L.C., Marrucho, I.M., 2017. Development of hydrophobic deep eutectic solvents for extraction of pesticides from aqueous environments. Fluid Phase Equilib. 448, 135–142. https://doi.org/10.1016/j.fluid.2017.04.002.

Florindo, C., Romero, L., Rintoul, I., Branco, L.C., Marrucho, I.M., 2018. From phase change materials to green solvents: hydrophobic low viscous fatty acid-based deep eutectic solvents. ACS Sustain. Chem. Eng. 6 (3), 3888–3895. https://doi.org/10.1021/acssuschemeng.7b04235.

Florindo, C., McIntosh, A.J.S., Welton, T., Branco, L.C., Marrucho, I.M., 2018. A closer look into deep eutectic solvents: exploring intermolecular interactions using solvatochromic probes. Phys. Chem. Chem. Phys. 20 (1), 206–213. https://doi.org/10.1039/C7CP06471C.

Florindo, C., Branco, L.C., Marrucho, I.M., 2019. Quest for green-solvent design: from hydrophilic to hydrophobic (Deep) eutectic solvents. ChemSusChem 12 (8), 1549–1559. https://doi.org/10.1002/cssc.201900147.
Francisco, M., Van Den Bruinhorst, A., Kroon, M.C., 2012. New Natural and renewable low transition temperature mixtures (LTTMs): screening as solvents for lignocellulosic biomass processing. Green Chem. 14 (8), 2153. https://doi.org/10.1039/c2gc35660k.
Fraser, K.J., MacFarlane, D.R., 2009. Phosphonium-based ionic liquids: an overview. Aust. J. Chem. 62 (4), 309–321. https://doi.org/10.1071/CH08558.
Gaboriau, F., Chéron, M., Leroy, L., Bolard, J., 1997. Physico-chemical properties of the heat-induced 'superaggregates' of amphotericin B. Biophys. Chem. 66 (1), 1–12. https://doi.org/10.1016/S0301-4622(96)02241-7.
Gano, Z.S., Mjalli, F.S., Al-Wahaibi, T., Al-Wahaibi, Y., AlNashef, I.M., 2017. Desulfurization of liquid fuel via extraction with imidazole-containing deep eutectic solvent. Green Process. Synth. 6 (5), 511–521. https://doi.org/10.1515/gps-2016-0124.
Ge, D., Wang, Y., Jiang, Q., Dai, E., 2019. A deep eutectic solvent as an extraction solvent to separate and preconcentrate parabens in water samples using in situ liquid-liquid microextraction. J. Braz. Chem. Soc. 30 (6), 1203–1210. https://doi.org/10.21577/0103-5053.20190014.
Golenser, J., Domb, A., 2006. New formulations and derivatives of amphotericin B for treatment of leishmaniasis. Mini-Rev. Med. Chem. 6 (2), 153–162. https://doi.org/10.2174/138955706775476037.
Gontrani, L., Russina, O., Lo Celso, F., Caminiti, R., Annat, G., Triolo, A., 2009. Liquid structure of trihexyltetradecylphosphonium chloride at ambient temperature: an X-ray scattering and simulation study. J. Phys. Chem. B 113 (27), 9235–9240. https://doi.org/10.1021/jp808333a.
Greaves, T.L., Kennedy, D.F., Mudie, S.T., Drummond, C.J., 2010. Diversity observed in the nanostructure of protic ionic liquids. J. Phys. Chem. B 114 (31), 10022–10031. https://doi.org/10.1021/jp103863z.
Grudzinski, W., Sagan, J., Welc, R., Luchowski, R., Gruszecki, W.I., 2016. Molecular organization, localization and orientation of antifungal antibiotic amphotericin B in a single lipid bilayer. Sci. Rep. 6 (1), 32780. https://doi.org/10.1038/srep32780.
Hammond, O.S., Bowron, D.T., Edler, K.J., 2016. Liquid structure of the choline chloride-urea deep eutectic solvent (reline) from neutron diffraction and atomistic modelling. Green Chem. 18 (9), 2736–2744. https://doi.org/10.1039/C5GC02914G.
Hansen, B.B., Spittle, S., Chen, B., Poe, D., Zhang, Y., Klein, J.M., Horton, A., Adhikari, L., Zelovich, T., Doherty, B.W., Gurkan, B., Maginn, E.J., Ragauskas, A., Dadmun, M., Zawodzinski, T.A., Baker, G.A., Tuckerman, M.E., Savinell, R.F., Sangoro, J.R., 2021. Deep eutectic solvents: a review of fundamentals and applications. Chem. Rev. 121 (3), 1232–1285. https://doi.org/10.1021/acs.chemrev.0c00385.
Hardacre, C., Holbrey, J.D., Mullan, C.L., Youngs, T.G.A., Bowron, D.T., 2010. Small angle neutron scattering from 1-alkyl-3-methylimidazolium hexafluorophosphate ionic liquids ([Cnmim][PF6], N=4, 6, and 8). J. Chem. Phys. 133 (7), 074510 https://doi.org/10.1063/1.3473825.
Huang, W., Zhang, Z., Han, X., Tang, J., Wang, J., Dong, S., Wang, E., 2002. Ion channel behavior of amphotericin B in sterol-free and cholesterol- or ergosterol-containing supported phosphatidylcholine bilayer model membranes investigated by electrochemistry and spectroscopy. Biophys. J. 83 (6), 3245–3255. https://doi.org/10.1016/S0006-3495(02)75326-5.
Jameson, L.P., Dzyuba, S.V., 2013. Circular dichroism studies on intermolecular interactions of amphotericin b in ionic liquid-rich environments. Chirality 25 (7), 427–432. https://doi.org/10.1002/chir.22142.
Juneidi, I., Hayyan, M., Mohd Ali, O., 2016. Toxicity profile of choline chloride-based deep eutectic solvents for fungi and cyprinus carpio fish. Environ. Sci. Pollut. Res. 23 (8), 7648–7659. https://doi.org/10.1007/s11356-015-6003-4.
Khataei, M.M., Yamini, Y., Nazaripour, A., Karimi, M., 2018. Novel generation of deep eutectic solvent as an acceptor phase in three-phase hollow fiber liquid phase microextraction for extraction and preconcentration of steroidal hormones from biological fluids. Talanta 178, 473–480. https://doi.org/10.1016/j.talanta.2017.09.068.
Latest Trends in Zoology and Entomology Sciences, 1st ed.; Deka, B., Ed.; AkiNik Publications, 2023; Vol. 14. https://doi.org/10.22271/ed.book.2219.
Leishmaniasis. https://www.who.int/health-topics/leishmaniasis (accessed 2023-08-19).
Li, C., Zhang, J., Li, Z., Yin, J., Cui, Y., Liu, Y., Yang, G., 2016. Extraction desulfurization of fuels with 'metal ions' based deep eutectic solvents (MDESs). Green Chem. 18 (13), 3789–3795. https://doi.org/10.1039/C6GC00366D.
Makoś, P., Słupek, E., Gębicki, J., 2020. Hydrophobic deep eutectic solvents in microextraction techniques–a review. Microchem. J. 152, 104384 https://doi.org/10.1016/j.microc.2019.104384.
Mannu, A., Blangetti, M., Baldino, S., Prandi, C., 2021. Promising technological and industrial applications of deep eutectic systems. Materials 14 (10), 2494. https://doi.org/10.3390/ma14102494.
Naik, P.K., Paul, S., Banerjee, T., 2019. Physiochemical properties and molecular dynamics simulations of phosphonium and ammonium based deep eutectic solvents. J. Solut. Chem. 48 (7), 1046–1065. https://doi.org/10.1007/s10953-019-00903-0.
OECD, 2021. Test Guideline No. 439: In Vitro Skin Irritation: Reconstructed Human Epidermis Test Methods.
Paiva, A., Craveiro, R., Aroso, I., Martins, M., Reis, R.L., Duarte, A.R.C., 2014. Natural deep eutectic solvents – solvents for the 21st century. ACS Sust. Chem. Eng. 2 (5), 1063–1071. https://doi.org/10.1021/sc500096j.
Patil, A.O., Bodige, S., 2016. Low Transition Temperature Mixtures or Deep Eutectic Solvents and Processes for Preparation Thereof. US20160122676A1.
Phelps, T.E., Bhawawet, N., Jurisson, S.S., Baker, G.A., 2018. Efficient and selective extraction of 99mTcO4– from aqueous media using hydrophobic deep eutectic solvents. ACS Sustain. Chem. Eng. 6 (11), 13656–13661. https://doi.org/10.1021/acssuschemeng.8b03950.
Pott, T., Méléard, P., 2009. New insight into the nanostructure of ionic liquids: a small angle X-Ray Scattering (SAXS) study on liquid tri-alkyl-methyl-ammonium bis (trifluoromethanesulfonyl)amides and their mixtures. Phys. Chem. Chem. Phys. 11 (26), 5469. https://doi.org/10.1039/b901582e.
Radošević, K., Cvjetko Bubalo, M., Gaurina Srček, V., Grgas, D., Landeka Dragičević, T., Radojčić Redovniković, I., 2015. Evaluation of toxicity and biodegradability of choline chloride based deep eutectic solvents. Ecotoxicol. Environ. Saf. 112, 46–53. https://doi.org/10.1016/j.ecoenv.2014.09.034.
Radošević, K., Čanak, I., Panić, M., Markov, K., Bubalo, M.C., Frece, J., Srček, V.G., Redovniković, I.R., 2018. Antimicrobial, cytotoxic and antioxidative evaluation of natural deep eutectic solvents. Environ. Sci. Pollut. Res. 25 (14), 14188–14196. https://doi.org/10.1007/s11356-018-1669-z.
Rajabi, M., Ghassab, N., Hemmati, M., Asghari, A., 2018. Emulsification microextraction of amphetamine and methamphetamine in complex matrices using an up-to-date generation of eco-friendly and relatively hydrophobic deep eutectic solvent. J. Chromatogr. A 1576, 1–9. https://doi.org/10.1016/j.chroma.2018.07.040.
Rajabi, M., Ghassab, N., Hemmati, M., Asghari, A., 2019. Highly effective and safe intermediate based on deep eutectic medium for carrier less-three phase hollow fiber microextraction of antiarrhythmic agents in complex matrices. J. Chromatogr. B 1104, 196–204. https://doi.org/10.1016/j.jchromb.2018.11.008.
Réeff, J., Gaignaux, A., Goole, J., De Vriese, C., Amighi, K., 2013. New sustained-release intraarticular gel formulations based on monolein for local treatment of arthritic diseases. Drug Dev. Ind. Pharm. 39 (11), 1731–1741. https://doi.org/10.3109/03639045.2012.730529.
Reichardt, C., 1994. Solvatochromic dyes as solvent polarity indicators. Chem. Rev. 94 (8), 2319–2358. https://doi.org/10.1021/cr00032a005.
Reithinger, R., Mohsen, M., Wahid, M., Bismullah, M., Quinnell, R.J., Davies, C.R., Kolaczinski, J., David, J.R., 2005. Efficacy of thermotherapy to treat cutaneous leishmaniasis caused by leishmania tropica in kabul, afghanistan: a randomized, controlled. Trial. Clin. Infect. Dis. 40 (8), 1148–1155. https://doi.org/10.1086/428736.
Reithinger, R., Dujardin, J.-C., Louzir, H., Pirmez, C., Alexander, B., Brooker, S., 2007. Cutaneous leishmaniasis. Lancet Infect. Dis. 7 (9), 581–596. https://doi.org/10.1016/S1473-3099(07)70209-8.
Rente, D., Cvjetko Bubalo, M., Panić, M., Paiva, A., Caprin, B., Radojčić Redovniković, I., Duarte, A.R.C., 2022. Review of deep eutectic systems from laboratory to industry, taking the application in the cosmetics industry as an example. J. Clean. Prod. 380, 135147 https://doi.org/10.1016/j.jclepro.2022.135147.
Ribeiro, B.D., Florindo, C.I.S., Iff, L., Coelho, M.A., Marrucho, I.M., 2015. Novel menthol-based eutectic mixtures: hydrophobic low viscosity solvents. ACS Sustain. Chem. Eng. 3 (10), 69–2477. https://doi.org/10.1021/acssuschemeng.5b00532.
Russina, O., Triolo, A., 2017. Ionic liquids and neutron scattering. In: Experimental Methods in the Physical Sciences. Elsevier, pp. 213–278. https://doi.org/10.1016/B978-0-12-805324-9.00004-2.
Rycerz, L., 2013. Practical remarks concerning phase diagrams determination on the basis of differential scanning calorimetry measurements. J. Therm. Anal. Calorim. 113 (1), 231–238. https://doi.org/10.1007/s10973-013-3097-0.
Santos, F., Leitão, P.S., Duarte, M.C.A., 2018. Properties of therapeutic deep eutectic solvents of L-arginine and ethambutol for tuberculosis treatment. Molecules 24 (1), 55. https://doi.org/10.3390/molecules24010055.
Schindelin, J., Arganda-Carreras, I., Frise, E., Kaynig, V., Longair, M., Pietzsch, T., Preibisch, S., Rueden, C., Saalfeld, S., Schmid, B., Tinevez, J.-Y., White, D.J., Hartenstein, V., Eliceiri, K., Tomancak, P., Cardona, A., 2012. Fiji: an open-source platform for biological-image analysis. Nat. Methods 9 (7), 676–682. https://doi.org/10.1038/nmeth.2019.
Schneider, C.A., Rasband, W.S., Eliceiri, K.W., 2012. NIH Image to ImageJ: 25 Years of Image Analysis. Nat. Methods 9 (7), 671–675. https://doi.org/10.1038/nmeth.2089.
Shishov, A.Y., Chislov, M.V., Nechaeva, D.V., Moskvin, L.N., Bulatov, A.V., 2018. A new approach for microextraction of non-steroidal anti-inflammatory drugs from human urine samples based on in-situ deep eutectic mixture formation. J. Mol. Liq. 272, 738–745. https://doi.org/10.1016/j.molliq.2018.10.006.
Siadat, A., Galehdari, H., Shahmoradi, Z., Iraji, F., Zolfaghari, A., Ansari, N., 2023. Treatment of cutaneous leishmaniasis with intense pulsed light: is it effective? Adv. Biomed. Res. 12 (1), 125. https://doi.org/10.4103/abr.abr_410_21.
Silva, A.L., 2017. Study of Amphotericin B Molecular Aggregation into Different Carrier System.
Smith, E.L., Abbott, A.P., Ryder, K.S., 2014. Deep Eutectic Solvents (DESs) and their applications. Chem. Rev. 114 (21), 11060–11082. https://doi.org/10.1021/cr300162p.
Song, X., Hamano, H., Minofar, B., Kanzaki, R., Fujii, K., Kameda, Y., Kohara, S., Watanabe, M., Ishiguro, S., Umebayashi, Y., 2012. Structural heterogeneity and unique distorted hydrogen bonding in primary ammonium nitrate ionic liquids studied by high-energy X-ray diffraction experiments and MD simulations. J. Phys. Chem. B 116 (9), 2801–2813. https://doi.org/10.1021/jp209561t.
Songkro, S., 2009. An overview of skin penetration enhancers: penetration enhancing activity, skin irritation potential and mechanism of action. Songklanakarin J. Sci. Technol. 31 (3), 299–321.
Tang, W., Dai, Y., Row, K.H., 2018. Evaluation of fatty acid/alcohol-based hydrophobic deep eutectic solvents as media for extracting antibiotics from environmental water. Anal. Bioanal. Chem. 410 (28), 7325–7336. https://doi.org/10.1007/s00216-018-1346-6.
Torrado, J.J., Espada, R., Ballesteros, M.P., Torrado-Santiago, S., 2008. Amphotericin B formulations and drug targeting. J. Pharm. Sci. 97 (7), 2405–2425. https://doi.org/10.1002/jps.21179.

Triolo, A., Russina, O., Caminiti, R., Shirota, H., Lee, H.Y., Santos, C.S., Murthy, N.S., Castner Jr, E.W., 2012. Comparing intermediate range order for alkyl- vs. ether-substituted cations in ionic liquids. Chem. Commun. 48 (41), 4959. https://doi.org/10.1039/c2cc31550e.

Van Osch, D.J.G.P., Zubeir, L.F., Van Den Bruinhorst, A., Rocha, M.A.A., Kroon, M.C., 2015. Hydrophobic deep eutectic solvents as water-immiscible extractants. Green Chem. 17 (9), 4518–4521. https://doi.org/10.1039/C5GC01451D.

Van Osch, D.J.G.P., Dietz, C.H.J.T., Van Spronsen, J., Kroon, M.C., Gallucci, F., Van Sint Annaland, M., Tuinier, R., 2019. A search for natural hydrophobic deep eutectic solvents based on natural components. ACS Sustain. Chem. Eng. 7 (3), 2933–2942. https://doi.org/10.1021/acssuschemeng.8b03520.

Wacha, A., 2015. Optimized pinhole geometry for small-angle scattering. J. Appl. Crystallogr. 48 (6), 1843–1848. https://doi.org/10.1107/S1600576715018932.

Wacha, A., Varga, Z., Bóta, A., 2014. CREDO: a new general-purpose laboratory instrument for small-angle X-ray scattering. J. Appl. Crystallogr. 47 (5), 1749–1754. https://doi.org/10.1107/S1600576714019918.

Wang, H., Hu, L., Liu, X., Yin, S., Lu, R., Zhang, S., Zhou, W., Gao, H., 2017. Deep eutectic solvent-based ultrasound-assisted dispersive liquid-liquid microextraction coupled with high-performance liquid chromatography for the determination of ultraviolet filters in water samples. J. Chromatogr. A 1516, 1–8. https://doi.org/10.1016/j.chroma.2017.07.073.

Waugh, C.D., 2007. Amphotericin B. In: xPharm: The Comprehensive Pharmacology Reference. Elsevier, pp. 1–5. https://doi.org/10.1016/B978-008055232-3.61226-7.

Wazeer, I., AlNashef, I.M., Al-Zahrani, A.A., Hadj-Kali, M.K., 2021. The subtle but substantial distinction between ammonium- and phosphonium-based deep eutectic solvents. J. Mol. Liq. 332, 115838 https://doi.org/10.1016/j.molliq.2021.115838.

Wortmann, G., Miller, R.S., Oster, C., Jackson, J., Aronson, N., 2002. A Randomized, double-blind study of the efficacy of a 10- or 20-day course of sodium stibogluconate for treatment of cutaneous leishmaniasis in United States military personnel. Clin. Infect. Dis. 35 (3), 261–267. https://doi.org/10.1086/341406.

Yang, D., Wang, Y., Peng, J., Xun, C., Yang, Y., 2019. A green deep eutectic solvents microextraction coupled with acid-base induction for extraction of trace phenolic compounds in large volume water samples. Ecotoxicol. Environ. Saf. 178, 130–136. https://doi.org/10.1016/j.ecoenv.2019.04.021.

Yusof, R., Abdulmalek, E., Sirat, K., Rahman, M., 2014. Tetrabutylammonium Bromide (TBABr)-Based Deep Eutectic Solvents (DESs) and their physical properties. Molecules 19 (6), 8011–8026. https://doi.org/10.3390/molecules19068011.

Zubeir, L.F., Van Osch, D.J.G.P., Rocha, M.A.A., Banat, F., Kroon, M.C., 2018. Carbon dioxide solubilities in decanoic acid-based hydrophobic deep eutectic solvents. J. Chem. Eng. Data 63 (4), 913–919. https://doi.org/10.1021/acs.jced.7b00534.